Enhanced Endo's approach for evaluating free-surface Green's function with application to wave-structure interactions

Liu, Yingyi
Research Institute for Applied Mechanics, Kyushu University

Cong, Peiwen
State Key Laboratory of Coastal and Offshore Engineering, Dalian University of Technology

Gou, Ying
State Key Laboratory of Coastal and Offshore Engineering, Dalian University of Technology

Yoshida, Shigeo
Research Institute for Applied Mechanics, Kyushu University

他

出版情報：Ocean Engineering. 207 (107377), 2020-07-01. Elsevier
バージョン：
権利関係：

Revised Manuscript (Unmarked)

Enhanced Endo's approach for evaluating free-surface Green's function with application to wave-structure interactions

Yingyi Liu[a], *Peiwen Cong*[b, *], *Ying Gou*[b], *Shigeo Yoshida*[a], *Masashi Kashiwagi*[c]

[a] Research Institute for Applied Mechanics, Kyushu University, Fukuoka 8168580, Japan

[b] State Key Laboratory of Coastal and Offshore Engineering, Dalian University of Technology, Dalian 116024, China

[c] Department of Naval Architecture & Ocean Engineering, Graduate School of Engineering, Osaka University, Osaka 5650871, Japan

Abstract

The Green function of the diffraction-radiation theory of time-harmonic waves under a moderate water depth is considered. The paper presents a newly developed enhanced algorithm based on Endo's approach, which employs a direct Gauss-Laguerre quadrature in the calculation of the principal value integrations. This methodology was firstly originated from Endo (1983), and had been subsequently improved by Liu et al. (2008) and Shan et al. (2018). Unfortunately, the latest version of Endo's approach still has two fatal problems with (1) incredibly large or small values at some "weird frequencies", and (2) nonsense values in the high-frequency region under a large depth. The present algorithm proposes special techniques for the removal of the singularities at these "weird frequencies", and provides special treatments to avoid exceeding hardware's limitation when the input parameter $k_0 h$ is overlarge. The developed algorithm is thereafter tested against a variety of sea conditions, via a comparison with Newman's polynomial algorithm (Newman, 1985), certifying its good accuracy in various circumstances. By carrying out a benchmark test on the DeepCwind semisubmersible, through a comparison with Shan's algorithm (Shan et al., 2018) and the commericial software Hydrostar®, the cause of the occurrence of the "weird frequencies" is found, in association with other important findings. The computations demonstrate that the present enhanced algorithm is thoroughly free from the preceding problems and is sufficiently accurate to compute wave loads in practice.

Keywords: free-surface Green's function; finite water depth; Gauss-Laguerre quadrature; diffraction-radiation theory; weird frequencies; ocean engineering; wave-structure interaction.

1. Introduction

Computational marine hydrodynamics has always been a good alternative to solve problems in ocean engineering that are overspent or not feasible to conduct laboratory experiments or onsite field tests. In recent years, marine structures (either floating or submarine) have been designed, planned and constructed towards an increasingly large scale owing to the rapid development of modern technologies. So far, wave interaction with such large structures over a wide-ranged selective sea states still needs to be analyzed using the boundary integral equation method (BIEM) based on the Laplacian equation, in association with some of the

* Corresponding author.
E-mail addresses: liuyingyi@riam.kyushu-u.ac.jp (Y. Liu), pwcong@dlut.edu.cn (P. Cong), gouying@dlut.edu.cn (Y. Gou), yoshidas@riam.kyushu-u.ac.jp (S. Yoshida), kashi@naoe.eng.osaka-u.ac.jp (M. Kashiwagi).

detailed investigations of the fluid field to be performed by a variety of computational fluid dynamics (CFD) methods based on the Navier-Stokes equations, due to the limitation of hardware's capabilities at present. The reason why BIEM is still being used widely is that it yields quite realistic and useful predictions. That is because all its unknowns are distributed solely on restricted specified boundaries, enabling the computational burden to be greatly reduced. At the meantime, BIEM can have a satisfactory accuracy for large-diameter structures in comparison to the wave lengths. In BIEM, the boundary integral equations are established based on Green's theorem within a confined or unconfined space (Mei et al., 2005), and are numerically solved by discretizing the boundaries into a large number of grids. In such a process, one of the most time-consuming parts is the evaluation of free-surface Green's function and its partial derivatives, the computation time of which increases quadratically with the number of unknowns on boundary surfaces, especially for structures with complex geometries. Generally speaking, a floating oil platform, an offshore wind turbine floating foundation, a submerged floating tunnel, or a large container vessel, consisting of $\mathcal{O}(10^3) \sim \mathcal{O}(10^4)$ number of panels, needs evaluations of the free-surface Green function and its partial derivatives in a number of $\mathcal{O}(10^6) \sim \mathcal{O}(10^8)$ times per wave frequency to compute linear wave loads. In case of computing second-order wave loads, mesh grids have to be even finer and therefore increase dramatically the times of evaluations of the Green function to an incredible number.

Computational techniques related to free-surface Green's function in infinite water depth have been well established by many scholars. Important works have been undertaken in developing rigorous formulations, effective algorithms & computer codes (e.g., Newman 1985, 1992; Telste and Noblesse, 1986; Ponizy et al., 1994; Chen 1993, 2004; Peter and Meylan, 2004; Clement, 2013; Wu et al., 2017; Shan and Wu, 2018; etc.). Worth noting is that, the idea originated from Noblesse (1982), focusing on a decomposition of the pulsating source into a wave component and a non-oscillatory local flow component, have turned into an open-source code published firstly by Telste and Noblesse (1986), improved by Ponizy et al. (1994), and later verified by Chakrabarti (2001). This work has been further simplified by Wu et al. (2017) recently, involving simply elementary functions for the local flow component, and does not require a division of the computational domain into multiple sub-domains. The algorithm of Wu et al. (2017) was validated subsequently by Liang et al. (2018) and improved further by Wu et al. (2018). A systematic description and comparison for the merits and the demerits of various numerical algorithms of the deep-water free-surface Green function have been recently given in Xie et al. (2018). Interested readers are referred to it for the more detailed information.

As been pointed out by Liu et al. (2018a), for some marine structures such as the substructures of marine renewble energy devices, since the designed water depths are of a moderate/intermediate scale ranging from approximately 20 meters to around 200 meters, considering the safety of the offshore structures, it is advisable and reasonable to use the finite-depth wave theory (Bayati et al., 2015) instead of assuming the installation water depth to be of infinity. However, the evaluation of free-surface Green's function in a finite depth is rather troublesome than that in an infinite depth due to the more complex singular nature of its

oscillating integrand. In general, the calculation strategies for such a finite-depth Green's function can be categorized into three types: (1) Extracting slow-varying components from the Green function and using a Chebyshev or multi-dimensional polynomial method to approximate them (e.g., Newman 1985, 1992; Chen 1993, 2004; etc.); (2) Applying asymptotic or power series expansions, such as eigenfunction expansions, rapid convergent series, or a combination with other numerical acceleration algorithms in different subregions (e.g., Pidcock, 1985; Linton, 1999; Liu et al., 2015, 2018a; etc.); (3) Decomposing the principal-value integral into two parts by subtracting a special term from the integrand and applying a direct Gauss-Laguerre quadrature to the numerical integration (e.g., Endo, 1983, 1987; Liu et al., 2008; Shan et al., 2019; etc.). The first two types of methods have been well established so far, while the third-type method which was firstly originated from Endo (1983) is still under development. This method was later applied by Li (2001) to interactions between two ships in waves. Thereafter, Liu et al. (2008) significantly improved Endo's approach by introducing a reduction of fraction and removing the singularity with the aid of infinite-depth Green's function and the exponential integral. Most recently, Shan et al. (2019) further improved Liu et al. (2008)'s method and summarized the algorithm in a systematical manner.

However, the latest version of Endo's approach, i.e., Shan's algorithm (Shan et al., 2019), still has fatal problems in application to the wave-structure interaction analysis. One problem is that, at some special frequencies, the computed wave hydrodynamic loads are surprisingly larger or smaller than those in the neighborhood, within a very limited frequency band, as shown in the following sections. This phenomenon is quite different from the known issue of "irregular frequencies" which is owing to the lack of a rigid lid on the waterplane area of a floating structure. Indeed, it is attributed to the inaccurate evaluation of the free-surface Green function by using a numerical integration method. For this reason, we name these special frequencies as "weird frequencies". This problem exists inherently in Endo's approach (Endo, 1987), which remains unsolved to date. Another problem is that in the circumstance of a large water depth or a high incident wave frequency, the computation results are always of *NaN* (Not a Number) values. To overcome these hurdles, the present work seeks a problem-shooting solution which can enhance Endo's approach. The remaining part of the paper is organized into the following sections: The background theory of wave-structure interactions is introduced in Section 2. The mathematical formulation of the enhanced algorithm involving special treatments are introduced in detail in Section 3. Verifications of the algorithm for a variety of sea conditions are given in Section 4.1. Application of the present algorithm to marine hydrodynamics of a complex floating structure is carried out in Section 4.2 where the cause of the occurrence of the "weird frequencies" is found. Conclusions are drawn in Section 5 based on the preceding analysis.

2. Theory of Wave-Structure Interactions Based on Boundary Integral Equations

Wave diffraction and radiation of an arbitrary-geometric three-dimensional floating structure can be solved by the boundary integral equation method. The method is based on the assumption that the fluid is

inviscid, incompressible, and with an irrotational motion. The fluid flow can be described by an ideal velocity potential satisfying the Laplace equation. By the use of Green's second identity, the following integral equation can be obtained:

$$C(\boldsymbol{x})\varphi_j(\boldsymbol{x}) + \iint_{S_B} \varphi_j(\boldsymbol{\xi}) \frac{\partial G(\xi;x)}{\partial n_\xi} \mathrm{d}S_\xi = \iint_{S_B} V(\xi) G(\xi;x) \mathrm{d}S_\xi \,,\ (j = 1\sim7, \boldsymbol{x} \in S_B, \boldsymbol{\xi} \in S_B), \tag{1}$$

where $\boldsymbol{x}$ and $\boldsymbol{\xi}$ represent the field point and the source point, respectively; $C(\boldsymbol{x})$ is referred to as "solid angle", whose value depends on the local geometric shape; $G(\boldsymbol{\xi}; \boldsymbol{x})$ is the free-surface Green function. The boundary condition on the immersed body surface S_B is impermeable and can be further represented by

$$V(\boldsymbol{\xi}) = \begin{cases} n_j(\boldsymbol{\xi}), & j = 1\sim6 \\ -\frac{\partial \varphi_0(\xi)}{\partial n_\xi}, & j = 7 \end{cases}, \tag{2}$$

where $n_j(\boldsymbol{\xi})$ stands for the normal derivatives on the geometrical surface and $\varphi_j(\boldsymbol{\xi})$ stands for (i) the incident wave potential when j =0, (ii) the radiation potentials when j =1~6, and (iii) the diffraction potential when j =7.

In Eq. (1), the free-surface Green's function $G(\boldsymbol{\xi}; \boldsymbol{x})$, or source potential, is usually defined as the velocity potential at the point (x, y, z) due to a point source of strength -4π located at the point (ξ, η, ζ), as shown in Fig. 1. Mathematically, it satisfies the following equation in the fluid domain,

$$\left(\frac{\partial^2}{\partial x^2} + \frac{\partial^2}{\partial y^2} + \frac{\partial^2}{\partial z^2}\right) G(x,y,z;\ \xi,\eta,\zeta) = \delta(x-\xi)(y-\eta)(z-\zeta) \tag{3}$$

subjecting to the corresponding boundary conditions

$$\left.\begin{array}{c} \frac{\partial G}{\partial z} = vG \quad z = 0 \\ \frac{\partial G}{\partial z} = 0 \quad z = -h \\ \lim_{R\to\infty}\left[\sqrt{vR}\left(\frac{\partial G}{\partial R} - \mathrm{i}vG\right)\right] = 0 \quad R \to \infty \end{array}\right\}, \tag{4}$$

where δ is the Dirac delta function, $v = \omega^2/g$ is the wave number in deep water, and R is the horizontal distance between the source and the field points. The last boundary condition in Eq. (4), referred to as the Sommerfeld radiation condition, shows that the pulsating potential decays with the horizontal distance and eventually vanishes in the far field. A rigorous theoretical solution to Eq. (3) and Eq. (4) has been found by John (1950), which can be expressed in the following form

$$G = \frac{1}{r} + \frac{1}{r_2} + 2\oint_0^\infty \frac{(k+v)\cosh k(z+h)\cosh k(\zeta+h)}{k\sinh kh - v\cosh kh} e^{-kh} J_0(kR)\mathrm{d}k, \tag{5}$$

where the path of the contour integral in Eq. (5) passes below the pole at $k = k_0$, in which k_0 is the positive real root of the water-wave dispersion equation; h is the water depth; r is the distance between the source and the field points, and r_2 is the distance between the field point and the image of the source point with respect

to the sea bottom. A Fortran subroutine (named 'Dispersion') has been recently developed in the open-source package FinGreen3D to obtain the accurate numerical solution of the dispersion equation (Liu et al., 2018a), using a higher-order iterative procedure as suggested by Newman (1990).

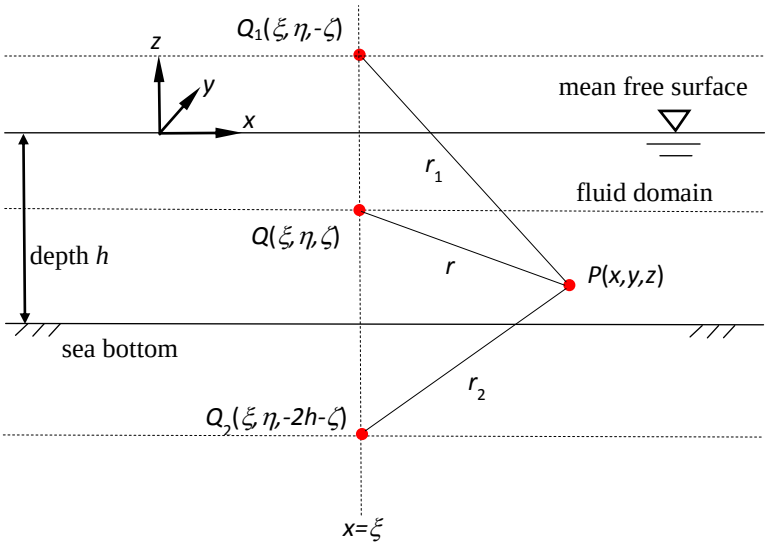

Fig. 1. Definition of the coordinate system in the three-dimensional space. *Q* denotes the pulsating source and *P* denotes the field point. Q_1 and Q_2 are the image points of *Q* with respect to the mean sea level and the seabed, respectively. (This figure is reproduced from Liu et al. (2018a))

3. An Improved Endo's Approach for Evaluation of Free-Surface Green's Function

3.1 Decomposition of Rankine sources and the wave term

Based on Eq. (5), the free-surface Green function can be expressed by

$$G = \frac{1}{r} + \frac{1}{r_2} + G_{Re} + G_{Im}, \tag{6}$$

where G_{Re} represents the real part (principal value) of the complex integral at the right-hand side of Eq. (5) and G_{Im} represents the imaginary part. Following the works of Endo (1987), Liu et al. (2008) and Shan et al. (2019), G_{Re} can be further decomposed into a summation of two terms

$$G_{Re} = PV \int_0^\infty \frac{2(k+\nu)\cosh k(\zeta+h)\cosh k(z+h)}{k\sinh kh - \nu\cosh kh} e^{-kh} J_0(kR)\mathrm{d}k = G_0 + G_1, \tag{7}$$

where

$$G_0 = \int_0^\infty e^{-kh}\bar{Q}(k)J_0(kR)\mathrm{d}k, \tag{8}$$

$$G_1 = PV \int_0^\infty \frac{2\nu+(k+\nu)e^{-2kh}}{(k\tanh kh-\nu)\left(1+e^{-2kh}\right)} e^{-kh}\bar{Q}(k)J_0(kR)\mathrm{d}k, \tag{9}$$

in which

$$\bar{Q}(k) = \sum_{i=1}^{4} \bar{Q}_i(k) = e^{k(\zeta+z+h)} + e^{-k(\zeta-z+h)} + e^{-k(z-\zeta+h)} + e^{-k(\zeta+z+3h)}. \quad (10)$$

Taking advantage of the following identity

$$\int_0^\infty e^{-\alpha x} J_0(\beta x)\mathrm{d}x = \frac{1}{\sqrt{\alpha^2+\beta^2}}, \quad (11)$$

G_0 can be simplified as a summation of four Rankine sources. Combining with the other two in Eq. (6), all the Rankine sources can be summarized into one single term, i.e.,

$$G_{Rankine} = \{R^2 + (z-\zeta)^2\}^{-1/2} + \{R^2 + (z+\zeta)^2\}^{-1/2} + \{R^2 + (z-\zeta-2h)^2\}^{-1/2} + \{R^2 + (z-\zeta+2h)^2\}^{-1/2} + \{R^2 + (z+\zeta+2h)^2\}^{-1/2} + \{R^2 + (z+\zeta+4h)^2\}^{-1/2}, \quad (13)$$

and Eq. (6) can be further expressed by

$$G = G_{Rankine} + G_1 + G_{Im}. \quad (14)$$

A good advantage of the above decomposition is that a majority of $1/r$-like weak singularities have been subtracted from the integral at the right-hand side of Eq.(5) and can therefore simplify the calculation of G_{Re}. Worth noting is that, in the constant panel method, these Rankine sources need to be integrated separately over each panel in the vicinity of that panel using an analytical algorithm (Newman, 1986), and numerically at some distance away using a Gaussian quadrature rule.

3.2 Numerical evaluation of the four integrations G_{1i} (i=1~4)

Let the denominator of the integrand in Eq. (9) be

$$g(k) = (k\tanh kh - v)\left(1 + e^{-2kh}\right), \quad (16)$$

$g(k)$ can be expanded using the Taylor expansion at the neighborhood of $k = k_0$, thereby keeps merely the linear approximation

$$g(k) \approx g(k_0) + (k-k_0)g'(k_0) = (k-k_0)[tanh(k_0h) + k_0hsech^2(k_0h)]\left(1 + e^{-2k_0h}\right). \quad (17)$$

The linear Taylor expansion is employed to subtract the singular integral kernel in the subsequent computations. Separating out each exponential function in Eq. (10) and combining them with Eq. (9), G_1 can be decomposed into four terms

$$G_1 = G_{11} + G_{12} + G_{13} + G_{14}. \quad (18)$$

According to Shan et al. (2019), due to the numerical distortion that is induced by Endo's formulation, it is better to arrange the right-hand side of Eq. (16) into two types of integrations, i.e., G_{11} and G_{1i} (i=2,3,4), which can be expressed as

$$G_{11} = \int_0^\infty e^{-kh}\left[\frac{f_{11}(k)}{g(k)} - \frac{f_{11}(k_0)}{(k-k_0)g'(k_0)}\right]e^{k(\zeta+z+h)}J_0(kR)\mathrm{d}k + PV\int_0^\infty \frac{f_{11}(k_0)}{(k-k_0)g'(k_0)}e^{k(\zeta+z)}J_0(kR)\mathrm{d}k, \quad (19)$$

where

$$f_{11}(k) = 2v + (k+v)e^{-2kh}, \tag{20}$$

and

$$G_{1i} = \int_0^\infty e^{-kh}\left[\frac{f_{1i}(k,R,z)}{g(k)} - \frac{f_{1i}(k_0,R,z)}{(k-k_0)g'(k_0)}\right]\mathrm{d}k + PV\int_0^\infty \frac{f_{1i}(k_0,R,z)e^{-kh}}{(k-k_0)g'(k_0)}\mathrm{d}k, \ (i=2,3,4), \tag{21}$$

where

$$f_{1i}(k) = [2v + (k+v)e^{-2kh}]\bar{Q}_i(k)J_0(kR). \tag{22}$$

The two types of formulations, i.e., Eq. (19) and Eq. (21), are quite different from each other mainly because of the principle-value integrations at their right-hand sides. In Eq. (19), the principle-value integration is finally deduced in terms of a special function $F(X,Y)$ which relates with the deep-water Green's function (Newman, 1985; Telste and Noblesse, 1986; Wu et al., 2017; etc.), while in Eq. (21), the principle-value integration is finally deduced in terms of the exponential integral $Ei(x)$. Applying a Gauss-Laguerre quadrature rule to the equations, Eq. (19) can be written as

$$G_{11} = \sum_{p=1}^{n}\frac{w_p}{h}\left[\frac{f_{11}(k_p)}{g(k_p)} - \frac{f_{11}(k_0)}{(k_p-k_0)g'(k_0)}\right]e^{k_p(\zeta+z+h)}J_0(k_pR) + F(X,Y)\frac{f_{11}(k_0)}{g'(k_0)}, \tag{23}$$

where $k_p = x_p/h$, and x_p is the *p*-th abscissa of the *n*-node Gauss-Laguerre quadrature rule, i.e., the *p*-th root of the *n*-th order Laguerre polynomial $L_n(x)$; $X = k_0R, Y = -k_0(z+\zeta)$, and

$$F(X,Y) = PV\int_0^\infty \frac{1}{k-1}e^{-kY}J_0(kX)\mathrm{d}k. \tag{24}$$

Eq. (21) can be written as

$$G_{1i} = \sum_{p=1}^{n}\frac{w_p}{h}\left[\frac{f_{1i}(k_p,R,z)}{g(k_p)} - \frac{f_{1i}(k_0,R,z)}{(k_p-k_0)g'(k_0)}\right] - e^{-k_0h}Ei(k_0h)\frac{f_{1i}(k_0,R,z)}{g'(k_0)}, \ (i=2,3,4). \tag{25}$$

Note that one should take care in the evaluation of the partial derivatives concerning the spatial coordinates *R* and *z*, which are therefore listed in detail in the Appendix.

3.3 Handling of the singularities for special-frequency incident waves

A numerical distortion occurs when the abscissa k_i approaches closely the positive real root k_0 of the dispersion equation, in Eq. (23) and Eq. (25). In such a case, the denominators of the two fractions in the square brackets are close to zeros, resulting in strong singularities. Take Eq. (23) for an example, that is to say, when $k_p \sim k_0$, there exist relationships of $g(k_p) \sim (k_p - k_0)g'(k_0) \approx 0$. Each fraction is therefore a ratio of two infinite small values. Certainly, the exact value of each fraction can be obtained via the L'Hôpital's rule, by differentiating simultaneously the nominator and the denominator with respect to *k*. An efficient simpler way is to set a conditional judgment that when $|k_p - k_0| < tol$, apply the following approximation:

$$\frac{f_{11}(k_p)}{g(k_p)} - \frac{f_{11}(k_0)}{(k_p - k_0)g'(k_0)} \sim \frac{f_{11}(k_p) - f_{11}(k_0)}{g(k_p)}, \tag{26}$$

where tol represents the tolerance, for which a value of 10^{-2} is recommended. An alternative way to do that is to apply an interpolation in between the narrow band of the singular region. Taking the linear interpolation for example, let

$$F_i(k) = \frac{f_{1i}(k,R,z)}{g(k)} - \frac{f_{1i}(k_0,R,z)}{(k-k_0)g'(k_0)}, \ (i=1,2,3,4), \tag{27}$$

and denote that the narrow band of the singular region is Δ, by calculating the values of $F_i(k)$ at the two bounds of the narrow band, the function value inside the singular region can be approximated by the linear interpolation

$$F_i(k) = [F_i(k_0 + \Delta) - F_i(k_0 - \Delta)](k - k_0)/(2\Delta) + F_i(k_0 - \Delta), \ (i=1, 2,3,4). \tag{28}$$

Using the above techniques, a large portion of weird points in the calculation results can be eliminated.

3.4 Special-treatment of the exponential integral for large parameters

In Eq. (25), the exponential integral $Ei(x)$ is defined by

$$Ei(x) = PV \int_{-\infty}^{x} \frac{e^t}{t} \mathrm{d}t, \tag{29}$$

in which the input parameter *x* is a positive real number. The integral in Eq. (29) should be understood in terms of the Cauchy principal value due to the singularity of the integrand at zero. Press et al. (2007) suggest a good algorithm to compute its principal value. Their strategy is to use the power series for small *x* and the asymptotic series for large *x*. When *x* is relatively small, the following power series can be applied:

$$Ei(x) = \gamma + \ln x + \sum_{n=1}^{\infty} \left(\frac{x^n}{n \cdot n!}\right), \tag{30}$$

where γ is Euler's constant. Indeed, Eq. (30) converges for any $x > 0$. However, when *x* is a large number, the power series converges very slow. To gain higher computational efficiency, an asymptotic expansion is recommended to use, with a form of

$$Ei(x) = \frac{e^x}{x}\left\{\sum_{n=0}^{N-1}\left(\frac{n!}{x^n}\right) + \mathcal{O}\left[\frac{N!}{(-x)^N}\right]\right\}, \tag{31}$$

where the second term in the square brackets represents the truncation error. A numerical problem occurs when *x* (the product of wave number and water depth) is too large for the exponential function e^x, leading to *NaN* values in a usual desktop or workstation computer. In such a case, a good solution is to calculate the exponential integral simultaneously with the exponential function $e^{-k_0 h}Ei(k_0 h)$ which appears in Eq. (25), formulated by

$$e^{-x}Ei(x) \sim \frac{1}{x}\sum_{n=0}^{N-1}\left(\frac{n!}{x^n}\right). \tag{32}$$

Through a combination usage of Eqs. (30) ~ (32), the numerical result concerning the exponential integral will no longer turn to be of nonsense values.

3.5 Improvements in calculating the hyperbolic functions in the high-frequency region

Except leading to nonsense values in the exponential integral, an overlarge value of k_0h (caused by either a large wave number or water depth), will result in another numerical distortion as well. It frequently happens in the high-frequency region of the computed hydrodynamic forces. The reason is similar to that of Eq. (31), because in calculating the incident wave potential and its derivatives, the value of the exponential function e^x exceeds hardware's limitation when the input parameter *x* is too large. Mathematically, the incident wave potential can be expressed as

$$\varphi_0 = -\frac{\mathrm{i}gA}{\omega}\frac{cosh[k_0(z+h)]}{cosh(k_0h)}e^{\mathrm{i}k_0(xcos\beta+ysin\beta)}, \tag{33}$$

where β is the wave heading angle. When k_0h is sufficiently large, since e^{-k_0h} is extremely small, Eq. (33) can be simplified as

$$\varphi_0 = -\frac{\mathrm{i}gA}{\omega}e^{k_0z}e^{\mathrm{i}k_0(xcos\beta+ysin\beta)}, \tag{34}$$

leading to a similar formulation to that of the infinite water depth except for the different wave number. Eq. (34) is no longer numerically unstable in computations and can, therefore, be used without any difficulty.

Similarly, this problem also occurs in the calculation of the imaginary part of Green's function. The imaginary part normally reads

$$G_{Im} = \frac{\pi}{N_0}cosh[k_0(\zeta+h)]cosh[k_0(z+h)]J_0(k_0R), \tag{35}$$

where the denominator N_0 is defined as

$$N_0 = \frac{h}{2}\left(1+\frac{\sinh 2k_0h}{2k_0h}\right). \tag{36}$$

An alternative expression for the factor π/N_0 can be derived as

$$\frac{\pi}{N_0} = \frac{2\pi v}{vh+\sinh^2 k_0h}. \tag{37}$$

However, when k_0h is sufficiently large, Eq. (35) is necessarily to be substituted by

$$G_{Im} = \frac{\pi(k_0+v)}{1+(k_0-v)h}e^{k_0(z+\zeta)}J_0(k_0R). \tag{38}$$

Derivatives of the incident potential and the imaginary part of Green's function can apply the same technique and are omitted here for brevity.

3.6 Tricks for speeding up the computation

Since the free-surface Green function needs to be evaluated in millions of times, any small improvement in the computational efficiency can help reduce the total time of the BIEM computation adequately. In the present algorithm, the codes are further optimized based on the following two principles:

(1) Minimize the number of times of evaluating the same functions. For instance, the exponential function $e^{-k_0 h}$ with frequent occurrences in the computation needs to be evaluated only once and stored in a variable, e.g., named `emk0h`. Thereafter, many other closely-related functions (e.g., $e^{-k_0(z+h)}$, $cosh[k_0(z+h)]$ and N_0, etc.) can be evaluated in terms of it, e.g., `emk0fh=exp(-k0*zf)*emk0h`, `ck0fh=(1.d0-emk0fh**2)/(2.d0*emk0fh)+emk0fh`, and `n0=h/2.d0*(1.d0+(1.d0-em4k0h)/(4.d0*k0*h*em2k0h))`, etc., in which $e^{-2k_0 h}$ and $e^{-4k_0 h}$ are again evaluated from `emk0h`, via `em2k0h=(emk0h)**2.d0`, `em4k0h=(em2k0h)**2.d0`. Another example is that, since the right-hand side of Eq. (20) is frequently calculated, a basic function can be defined as

$$q = [2v + (k+v)e^{-2kh}]. \tag{39}$$

The function only needs to be evaluated once and stored for calculation of other functions like $f_{1i}(k)$, (i=1~4), etc., to reduce the computation effort.

(2) Use polynomials and simple arithmetic operations in the calculation of some complicated special functions, e.g., the Bessel functions, exponential integral functions, etc. These special functions can be evaluated using specialized algorithms, e.g., those from the book of Zhang and Jin (1996) based on simple continued fractions. In this way, all the calculations in the code contain only arithmetic operations, which therefore greatly speeds up the computation.

4. Results and Discussions

4.1 Verifications of the present algorithm

Comparison between the present algorithm, Shan's algorithm (Shan et al., 2019) and Newman's algorithm (Newman, 1985) are made, as shown in Figs. 2 ~ 4, in the calculation of the Green function's value and derivatives. The pulsating source point and the fluid field point are chosen to be located in various places, at the free surface or underneath. The water depth varies from a small value, e.g., 2m, to a large value over 200m. The horizontal radius R also varies from the neighborhood of the source point to a far field where the local disturbance of waves diminishes. It is shown that, under various conditions, perfect agreements can always be achieved between the present results and those applying Newman's algorithm. However, the results produced by Shan's algorithm (Shan et al., 2019) have discrepancies between those from Newman's algorithm and the present. At some critical frequencies, results of Shan's algorithm (Shan et al., 2019) show rather strange values, having either sharp leaps or declines, within a very short frequency band. For brevity,

these frequencies are named as “weird frequencies” in the following sections. The reason for the occurrence of these frequencies will be further elucidated in the subsequent analysis.

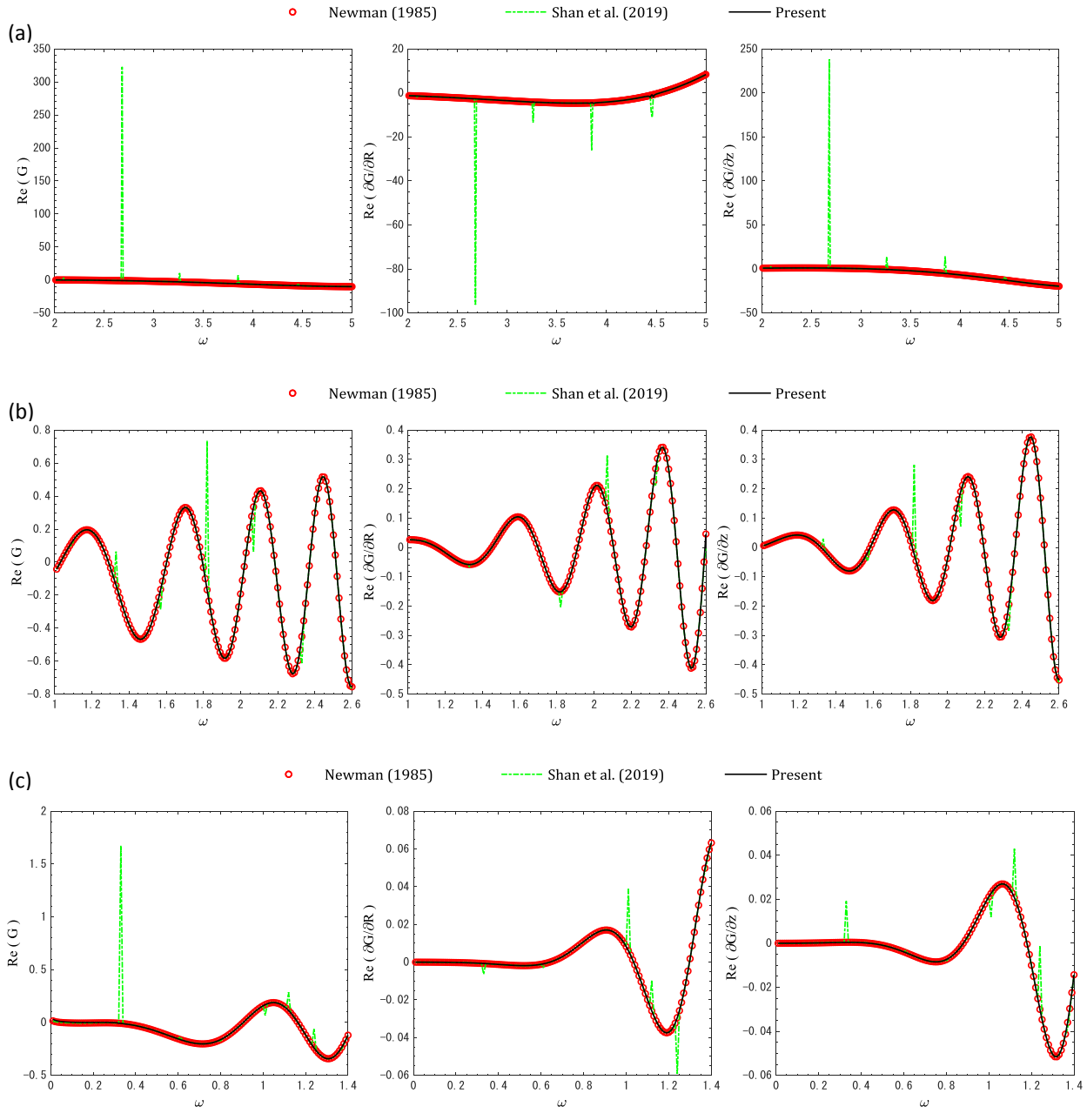

Fig. 2. Comparisons of free-surface Green’s function G and its partial gradient ∇G, as a function of wave angular frequency ω, when both of the field point and the source point are located at the free surface: (a) h = 5.0 m, R = 1.0 m, z = 0.0 m, ζ = 0.0 m; (b) h = 30.0 m, R = 40.0 m, z = 0.0 m, ζ = 0.0 m; (c) h = 200.0 m, R = 50.0 m, z = 0.0 m, ζ = 0.0 m. The red solid-circle line stands for results evaluated using Newman (1985)’s polynomial approximation; the green dash-dotted line stands for those evaluated using Shan et al. (2019)’s method; the black solid line stands for the present results.

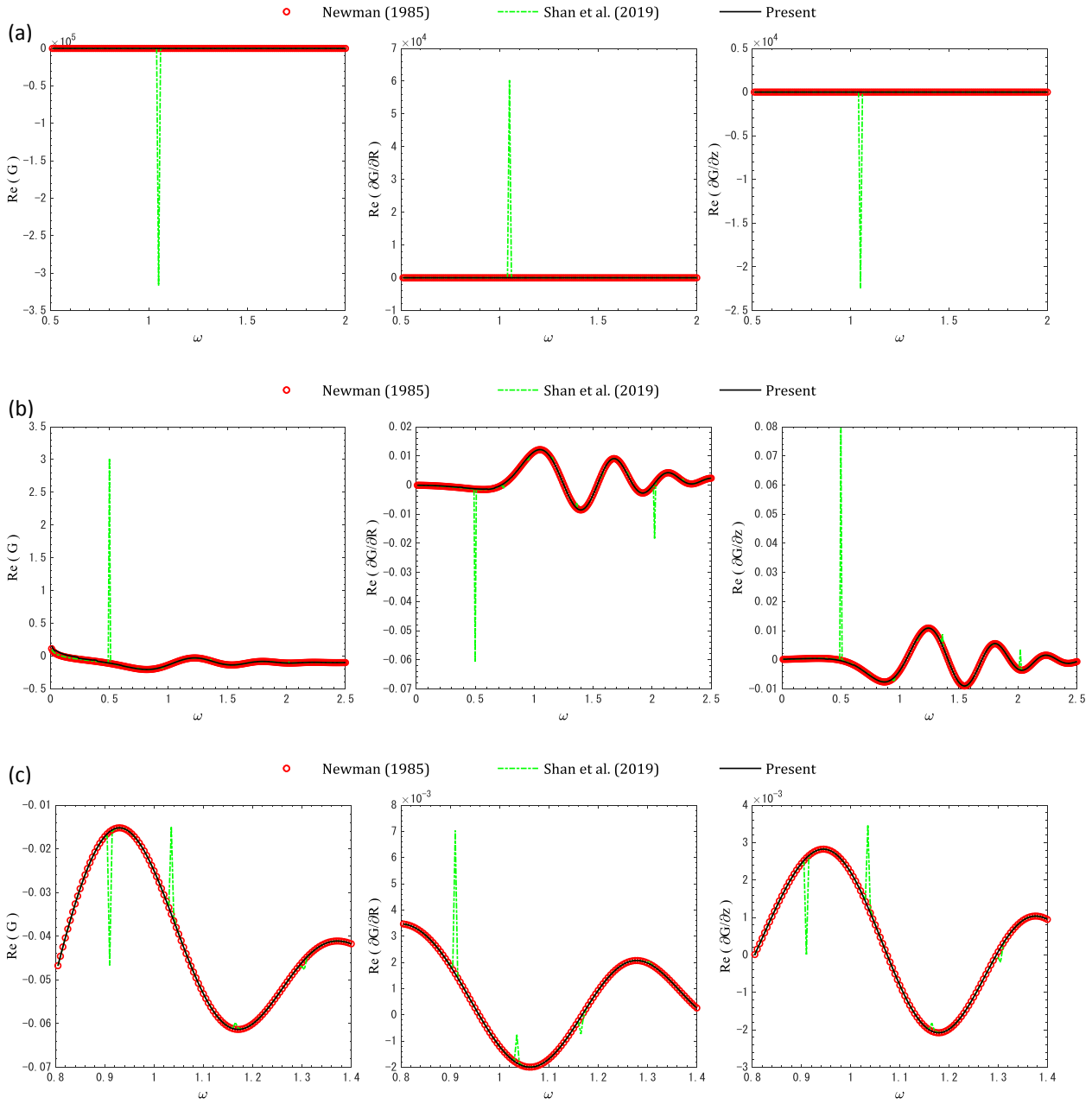

Fig. 3. Comparisons of free-surface Green's function G and its partial gradient ∇G, as a function of wave angular frequency ω, when either the field point or the source point is located at the free surface: (a) h = 2.0 m, R = 5.0 m, z = -0.8 m, ζ = 0.0 m; (b) h = 40.0 m, R = 35.0 m, z = 0.0 m, ζ = -10.0 m; (c) h = 120.0 m, R = 60.0 m, z = -20.0 m, ζ = 0.0 m. Description of the line types is given in Fig. 2.

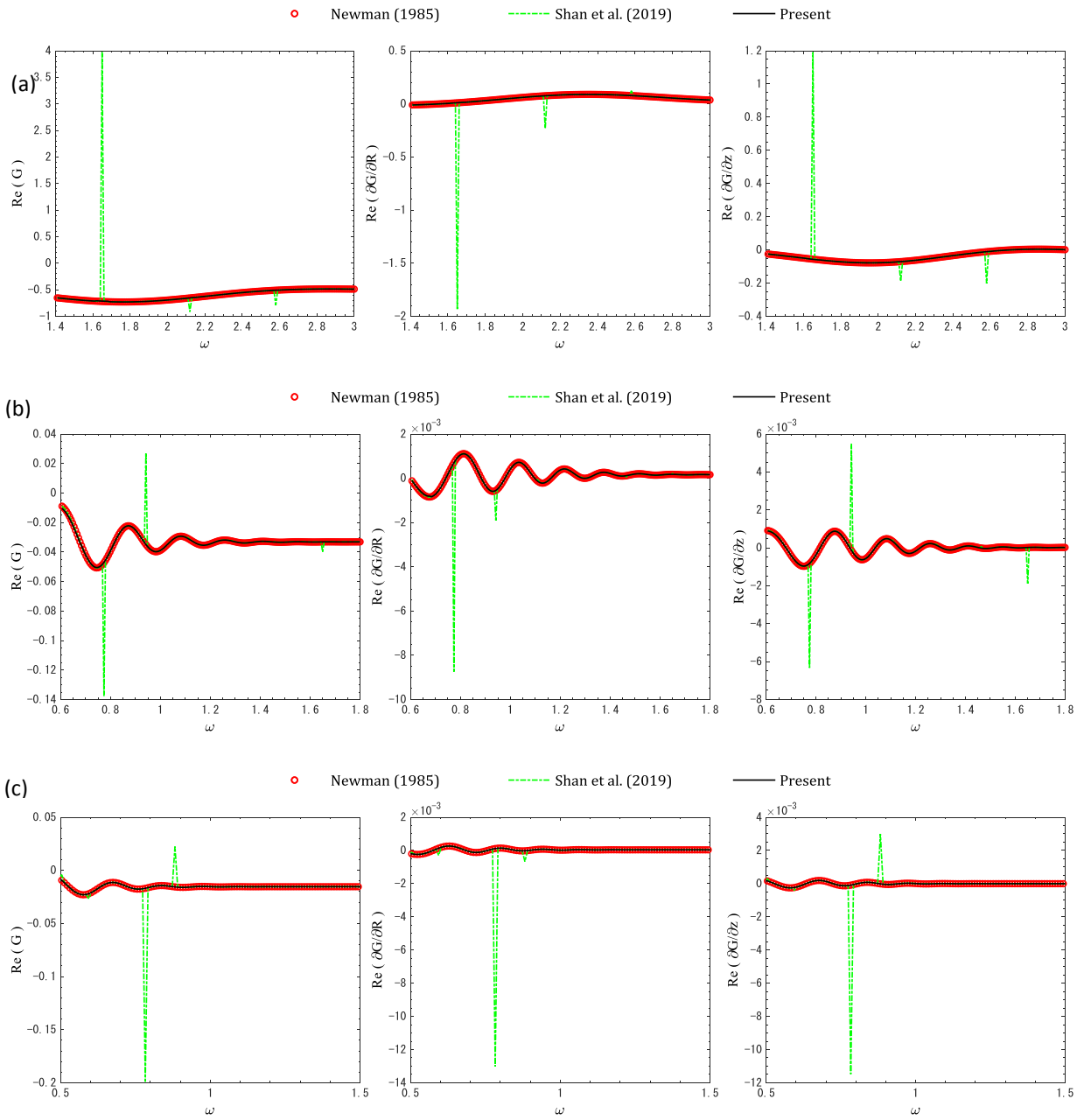

Fig. 4. Comparisons of free-surface Green's function G and its partial gradient ∇G, as a function of wave angular frequency ω, when both of the field point and the source point are located on the immersed body surface: (a) h = 8.0 m, R = 6.0 m, z = -2.0 m, ζ = -3.0 m; (b) h = 60.0 m, R = 150.0 m, z = -10.0 m, ζ = -20.0 m; (c) h = 210.0 m, R = 250.0 m, z = -20.0 m, ζ = -40.0 m. Description of the line types is given in Fig. 2.

4.2 Convergence tests against the quadrature order

As one may note, the first integral at the right-hand side of Eq. (19) involves an exponential term $e^{k(\zeta+z)}$, which vanishes when $\zeta + z = 0$, i.e., both of the source point and the field point are located at the free surface. In such a case, taking consideration of the asymptotic form of the Bessel function, the integrand of the first integral in Eq. (19) is of order $\mathcal{O}\left(k^{-3/2}\right)$ when k tends to infinity, and the integrand of the space

derivatives of G_{11} in Eqs. (A4) and (A5) are of order $\mathcal{O}\left(k^{-1/2}\right)$. Although the Gauss-Laguerre quadrature may still apply (Wikipedia, 2020), it is better to check the numerical stability of the integral. Therefore, a convergence test is performed against the quadrature order in calculation of the term G_{11}, as shown in Fig. 5. The quadrature rules of 8, 15, 30, 40 and 100 points are respectively chosen to evaluate the Green function and the spatial derivatives at the free surface over a wide range of water depths and horizontal distances. Good agreements between the results are found showing that Gauss-Laguerre quadrature does converge with respect to the quadrature order. In addition, it is shown that even a small number of quadrature points, i.e., an 8-node Gauss-Laguerre rule is sufficient for the calculation.

(a)

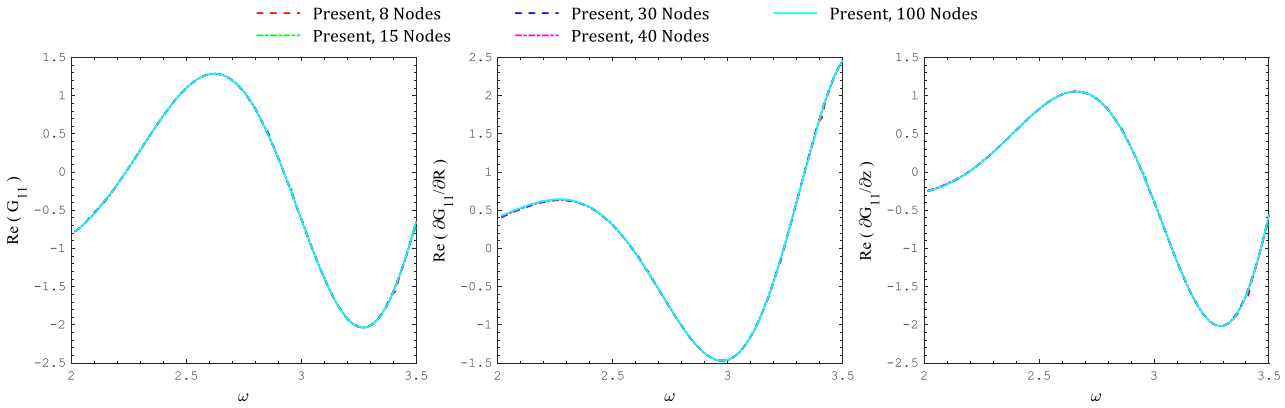

(b)

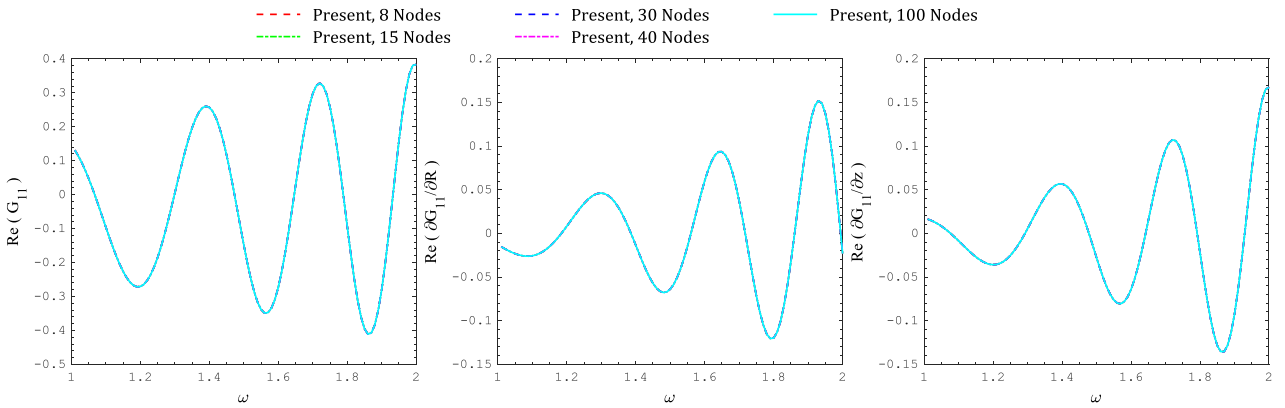

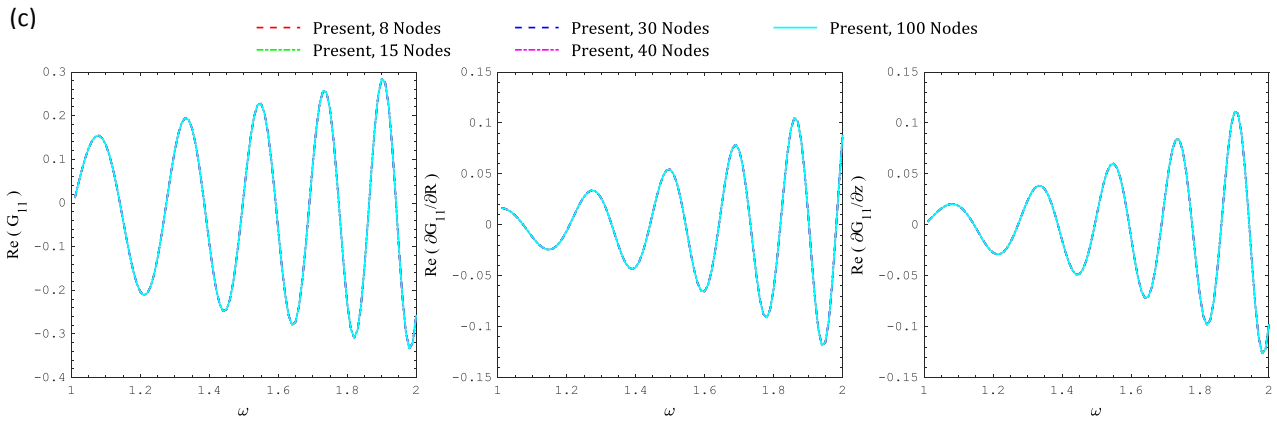

Fig. 5. Convergence test for the present algoritm against the quadrature order in calculation of the term G_{11}, as a function of wave angular frequency ω, when both of the field point and the source point are located at the free surface: (a) h = 6.0 m, R = 8.0 m, z = 0.0 m, ζ = 0.0 m; (b) h = 50.0 m, R = 60.0 m, z = 0.0 m, ζ = 0.0 m; (c) h = 150.0 m, R = 100.0 m, z = 0.0 m, ζ = 0.0 m.

4.3 Computation efficiency of the present algorithm

Fig. 6 shows the CPU time (unit: μs) of per evaluation of the Green's function and its derivatives using the present algorithm and the open-source code FinGreen3D (Liu et al., 2018a), on a desktop machine with an Intel(R) Xeon(R) E5-2620 v3 CPU of 2.40 GHz. The computations are performed sequentially on one single thread and the CPU times are obtained based on the average time of 0.2 billion evaluations of each code at each point distance R/h. Fig. 6 shows that one implementation of the present algorithm, i.e., per evaluation of the Green function and its derivatives consumes approximately 1.8~2.7 μs. Note that the computation time of the open-source code FinGreen3D (Liu et al., 2018a) varies significantly over R/h, while the present algorithm is less affected by the parameter R/h. In the lower R/h region, the present algorithm is superior to FinGreen3D (Liu et al., 2018a) and vice versa in the higher R/h region. A good way to improve the computational efficiency of the present algorithm in the higher R/h region is to apply a combination with the eigenfunction expansion method. An appropriate threshold value for the parameter R/h is 1.8, unlike 0.5 that has been suggested by Newman (1985), based on the comparison shown in Fig. 6. With such a combination, the computation time can be substantially reduced throughout the entire region of R/h.

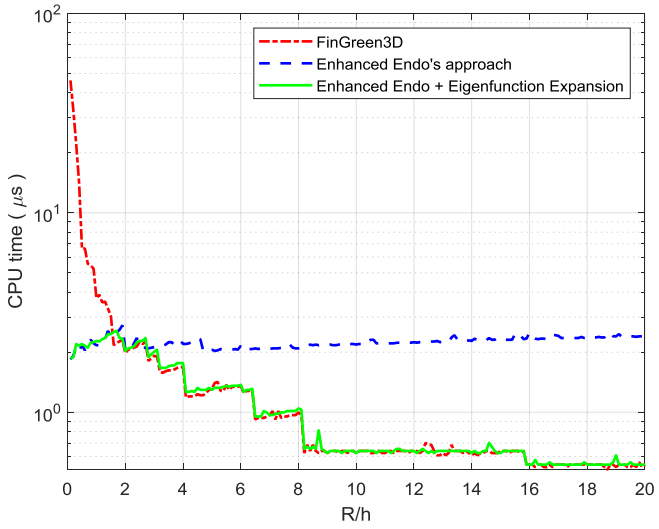

Fig. 6. Computation time for per implementation of the open-source code FinGreen3D (Liu et al., 2018a), the present algorithm and its combination with the eigenfunction expansion method, as a function of the normalized point distance R/h. The figure is obtained based on the averaged CPU time of 1 million evaluations of the codes respectively for each point distance R/h.

4.3 Application to Waves-Structure Interactions

The present algorithm and Shan's algorithm (Shan et al., 2019) are therefore programmed into computer subroutines and successfully interfaced to a wave-structure-interaction panel code HAMS (Hydrodynamic Analysis of Marine Structures) (Liu et al., 2016; Liu, 2019), respectively. In the subsequent computations, the computer codes are compiled by the Intel® Fortran Compiler (IFORT) Version 18.0.5.274.

To illustrate the capabilities of the present algorithm and its advantages over the previous algorithm in the wave-structure interaction analysis, a complex semisubmersible platform is presented as a numerical test for the validation. The platform is the floating foundation of the OC4 DeepCwind semisubmersible floating wind turbine, as shown in Fig. 7. The platform consists of a central column, three outer offset columns and a host of slender bracings to connect between the columns making the floating structure sufficient stiff. Geometrical specifications of the DeepCwind semi-submersible are listed in Table 1. More details can be found in Robertson et al. (2014).

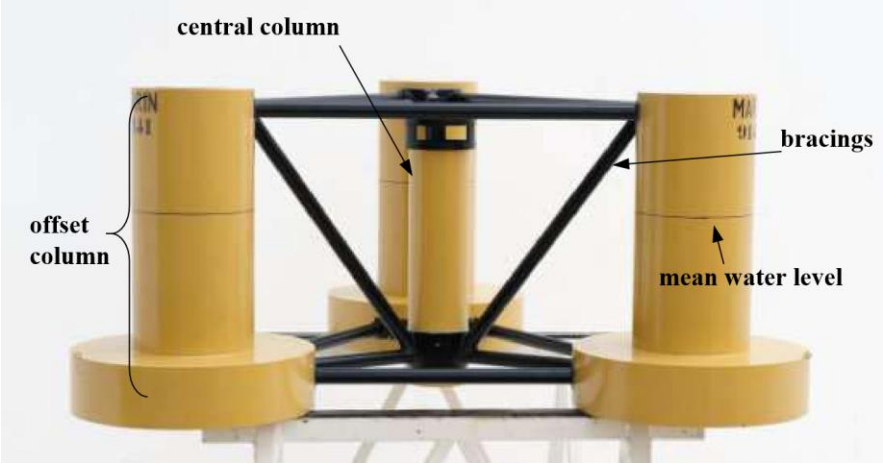

Fig. 7. Floating foundation of the OC4 DeepCwind semisubmersible floating wind turbine (Robertson et al., 2014; Benitz et al., 2015).

Table 1. Geometrical specifications of the DeepCwind semisubmersible platform (Robertson et al., 2014; Liu et al., 2018b).

Platform Properties	Value
Platform draft	20.0 m
Centerline spacing between offset columns	50.0 m
Length of upper columns	26.0 m
Length of base columns	6.0 m
Diameter of main column	6.5 m
Diameter of offset (upper) columns	12.0 m
Diameter of base columns	24.0 m
Diameter of pontoons and cross braces	1.6 m

Hydrodynamic mesh is generated only for the immersed part of the platform, and the waterplane at the cross-sections of the columns intersecting the mean sea surface. Based on a convergence test, around 3000 panels are chosen as an appropriate number of panels for the subsequent computations, as displayed in Fig. 8. Each of the three footings is discretized into $38\times8\times4$ constant panels (38 in circumferential, 8 in radial and 4 in vertical directions) of a quadrilateral or triangular element type. Each of the three outer offset columns and the central column are discretized into $20\times5\times8$ panels and $12\times3\times12$ panels, respectively. The bracings are meshed by sufficient dense panels as well. A symmetry plane *x*-*z* is applied to reduce remarkably the computation time. Computation results using the same hydrodynamic mesh from a well-recognized commercial software Hydrostar® are also given to validate the present numerical results.

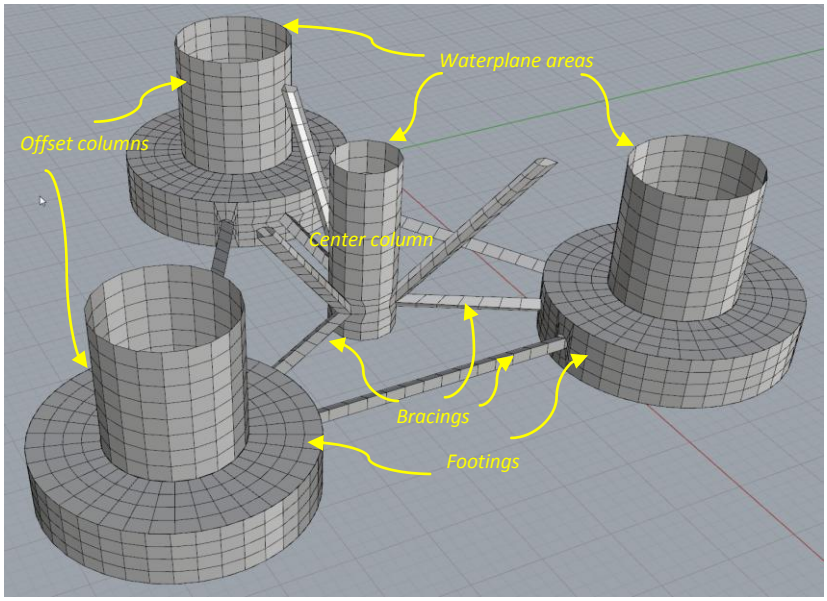

Fig. 8. The hydrodynamic mesh (visualized by the commercial software Rhinoceros® Version 5) of the immersed part of the DeepCwind semisubmersible, as an input to Hydrostar® and HAMS (Liu, 2019) in the computation.

4.3.1 Effect of the quadrature order of the Gauss–Laguerre rule in the evaluation of integrations

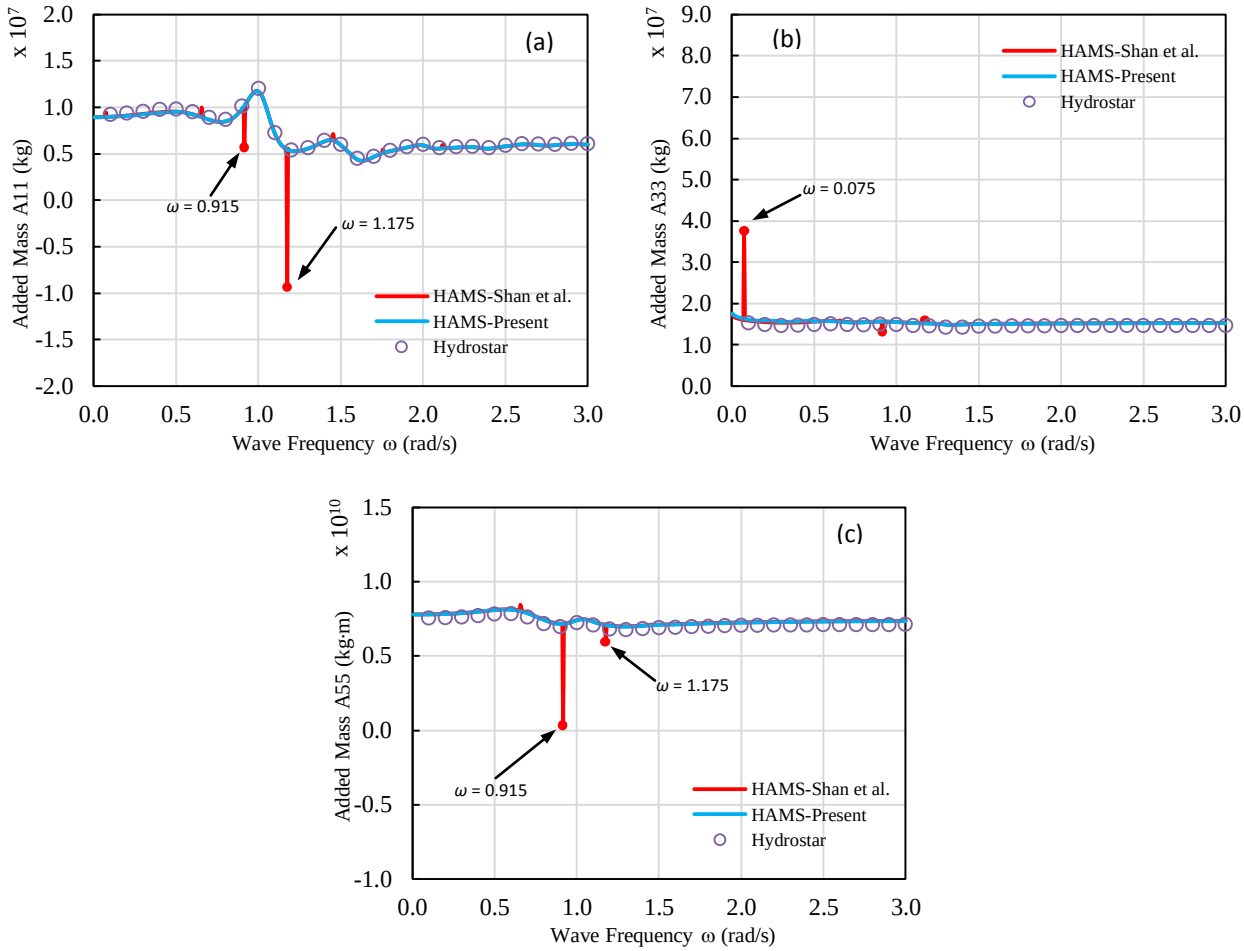

Fig. 9. Added mass of the DeepCwind semisubmersible, as a function of the wave angular frequency ω: (a) surge added mass, (b) heave added mass and (c) pitch added mass. In this figure, 8 Gauss–Laguerre nodes are used in evaluating the integrals of Green's function, in both of Shan's algorithm (Shan et al., 2019) and the present. The results denoted as "Hydrostar" are computed using the commercial software Hydrostar®.

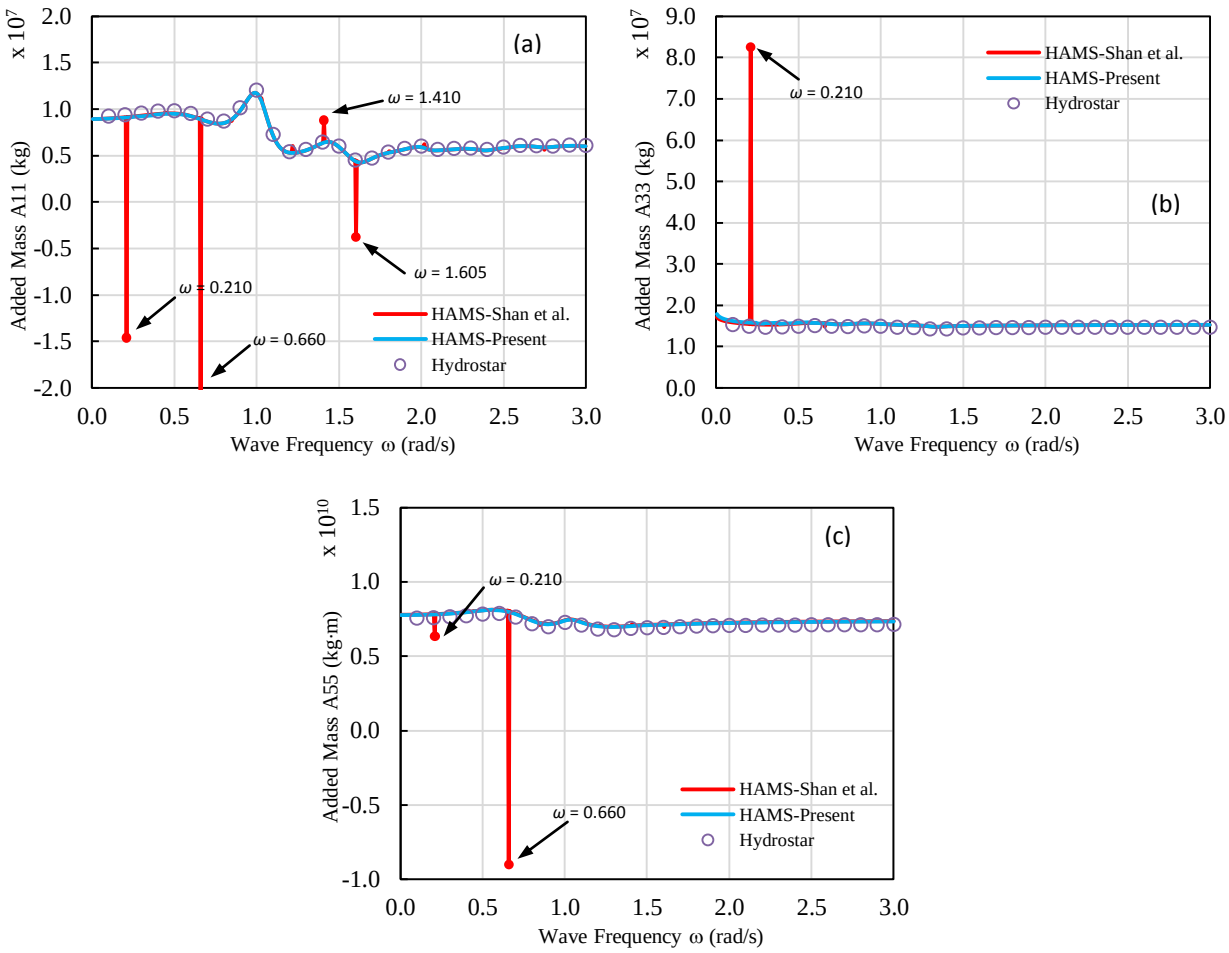

Fig. 10. Added mass of the DeepCwind semisubmersible, as a function of the wave angular frequency ω: (a) surge added mass, (b) heave added mass and (c) pitch added mass. In this figure, 15 Gauss–Laguerre nodes are used in evaluating the integrals of Green's function, in both of Shan's algorithm (Shan et al., 2019) and the present. The results denoted as "Hydrostar" are computed using the commercial software Hydrostar®.

Fig. 9 and 10 show the computation results of the added mass of a floating body (the DeepCwind semisubmersible) by HAMS (Liu, 2019), where the free-surface Green function is calculated respectively by Shan's algorithm (Shan et al., 2019) and the present. As a comparison, results computed by Hydrostar® are displayed as well. 8–node and 15–node Gauss–Laguerre quadrature rules have been applied respectively in the calculation of the four types of integrations G_{1i} (i =1~4) in Fig. 9 and 10. The abscissas of the 8–node and 15–node Gauss–Laguerre quadrature rules are displayed respectively in Table 2 and 3, in association with the wave numbers and the wave angular frequencies in correspondence. It appears that the weird frequencies

found in Fig. 9 and 10 due to the use of Shan's algorithm (Shan et al., 2019) are rather close to some of the frequency abscissas in Table 2 and 3, respectively. At these weird frequencies, the computation results by Shan's algorithm (Shan et al., 2019) show abnormal peaks, while those from the present algorithm are free from such a problem. The reason of the unstable results by Shan's algorithm (Shan et al., 2019) is that, when the wave frequency gets close to the real positive root k_0 of the dispersion equation, the denominators of the two fractions in the square brackets of Eq. (19) become strongly singular. It is noted that, the loci of the weird frequencies vary with the order of the quadrature rule. These conclusions hold for the radiation damping and the wave excitation force as well. The singularities in the denominator of the integrands of Eq. (23) and Eq. (25) are shown in Table 2 and 3.

Table 2. Abscissas of the 8-node Gauss-Laguerre quadrature in the calculation of the integrations G_{1i} (i =1~4)

p	x_p	$k_p = x_p/h$	$\omega_p = \sqrt{g k_p \tanh(k_p h)}$
1	0.170280	0.003406	0.075063
2	0.903702	0.018074	0.356823
3	2.251087	0.045022	0.657251
4	4.266700	0.085334	0.914766
5	7.045905	0.140918	1.175757
6	10.758516	0.215170	1.452866
7	15.740679	0.314814	1.757362
8	22.863132	0.457263	2.117958

Table 3. Abscissas of the 15-node Gauss-Laguerre quadrature in the calculation of the integrations G_{1i} (i =1~4)

p	x_p	$k_p = x_p/h$	$\omega_p = \sqrt{g k_p \tanh(k_p h)}$
1	0.093308	0.001866	0.041270
2	0.492692	0.009854	0.210032
3	1.215595	0.024312	0.447154
4	2.269950	0.045399	0.660270
5	3.667623	0.073352	0.847732
6	5.425337	0.108507	1.031702
7	7.565916	0.151318	1.218373
8	10.120229	0.202405	1.409109
9	13.130282	0.262606	1.605042
10	16.654408	0.333088	1.807649
11	20.776479	0.415530	2.018996
12	25.623894	0.512478	2.242188
13	31.407519	0.628150	2.482369
14	38.530683	0.770614	2.749495
15	48.026086	0.960522	3.069645

4.3.2 Effect of the frequency step size in the computation using boundary element method

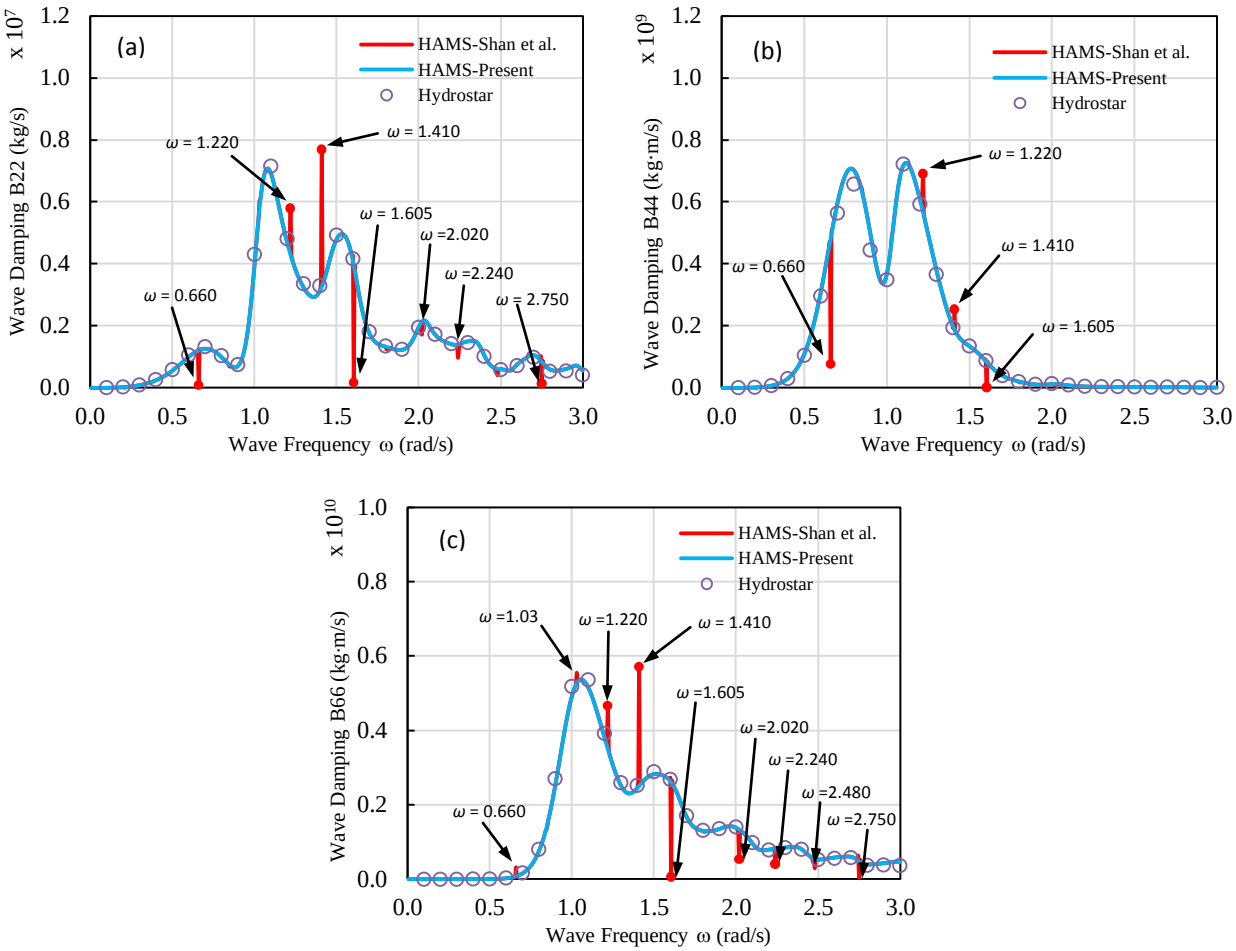

Fig. 11. Radiation damping of the DeepCwind semisubmersible, as a function of the wave angular frequency ω: (a) sway radiation damping, (b) roll radiation damping and (c) yaw radiation damping. In this figure, the frequency step is $\Delta\omega = 0.005\ rad/s$, in both of Shan's algorithm (Shan et al., 2019) and the present. The results denoted as "Hydrostar" are computed using the commercial software Hydrostar®.

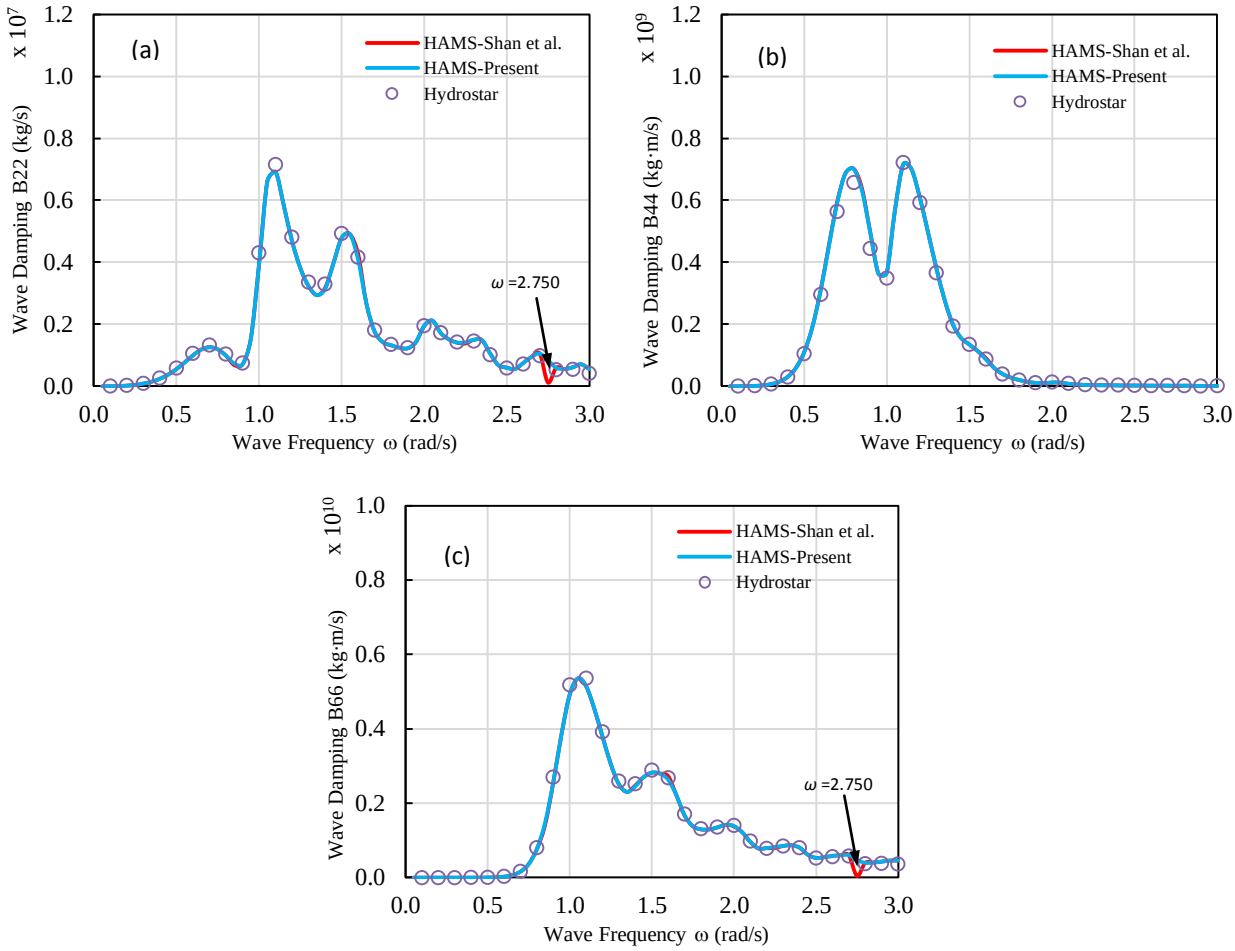

Fig. 12. Radiation damping of the DeepCwind semisubmersible, as a function of the wave angular frequency ω: (a) sway radiation damping, (b) roll radiation damping and (c) yaw radiation damping. In this figure, the frequency step is $\Delta\omega = 0.05\ rad/s$, in both of Shan's algorithm (Shan et al., 2019) and the present. The results denoted as "Hydrostar" are computed using the commercial software Hydrostar®.

Fig. 11 and 12 show the computation results of the radiation damping of the DeepCwind semisubmersible by HAMS (Liu, 2019), applying respectively Shan's algorithm (Shan et al., 2019) and the present in evaluating the Green function. In the computations, a frequency step of $\Delta\omega$=0.005 rad⁄s has been applied in Fig. 11 and $\Delta\omega$=0.05 rad⁄s in Fig. 12, respectively. It is found that the computational results are quite sensitive to the size of the frequency step. The contaminated frequency band in the computed wave loads is substantially affected by the frequency step. Applying a relatively large frequency step can (though may not completely) help to avoid the occurrence of the weird frequencies inherent in Shan's algorithm (Shan et al., 2019). On the other way, a small frequency is helpful to identify the loci of these weird frequencies. These conclusions hold for the added mass and the wave excitation force as well.

4.3.3 Effect of large parameters in the high-frequency region of wave hydrodynamics

(a)

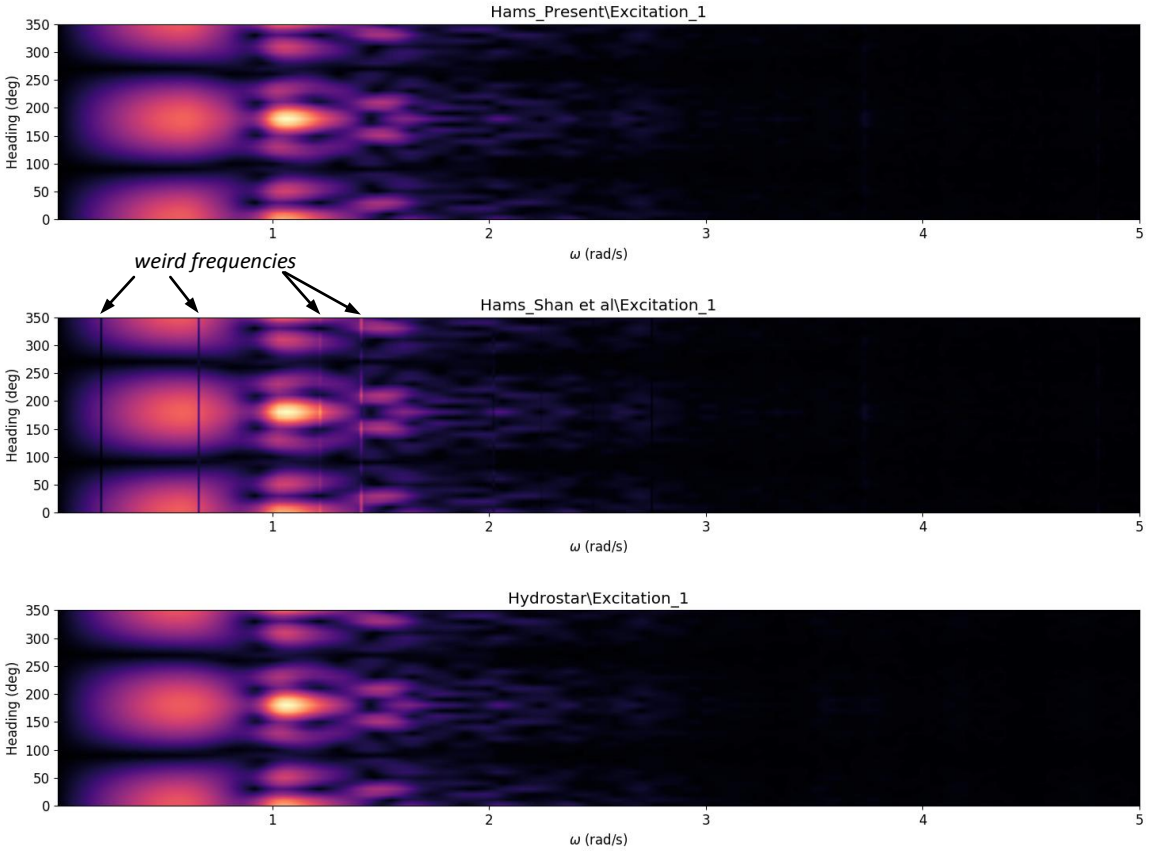
Hams_Present\Excitation_1
Heading (deg)
ω (rad/s)
weird frequencies
Hams_Shan et al\Excitation_1
Heading (deg)
ω (rad/s)
Hydrostar\Excitation_1
Heading (deg)
ω (rad/s)

(b)

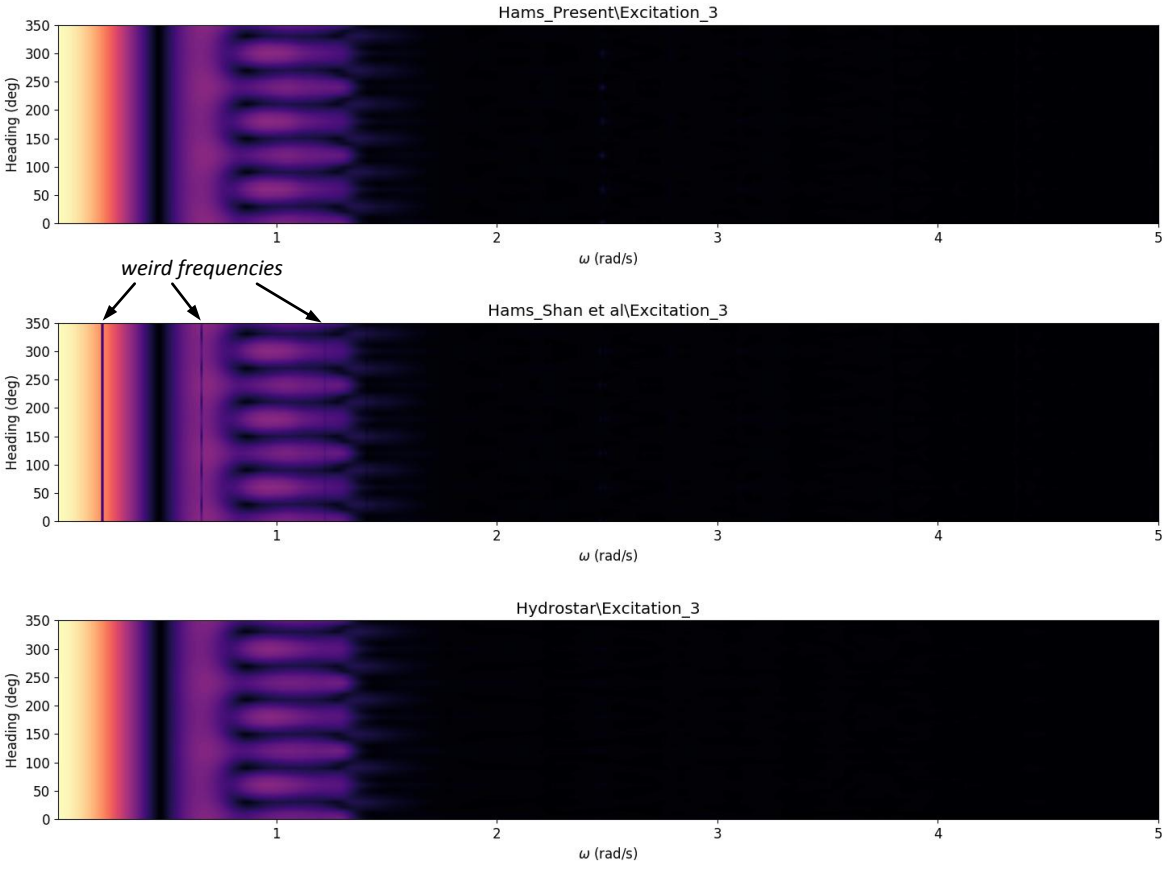
Hams_Present\Excitation_3
Heading (deg)
ω (rad/s)
weird frequencies
Hams_Shan et al\Excitation_3
Heading (deg)
ω (rad/s)
Hydrostar\Excitation_3
Heading (deg)
ω (rad/s)

(c)

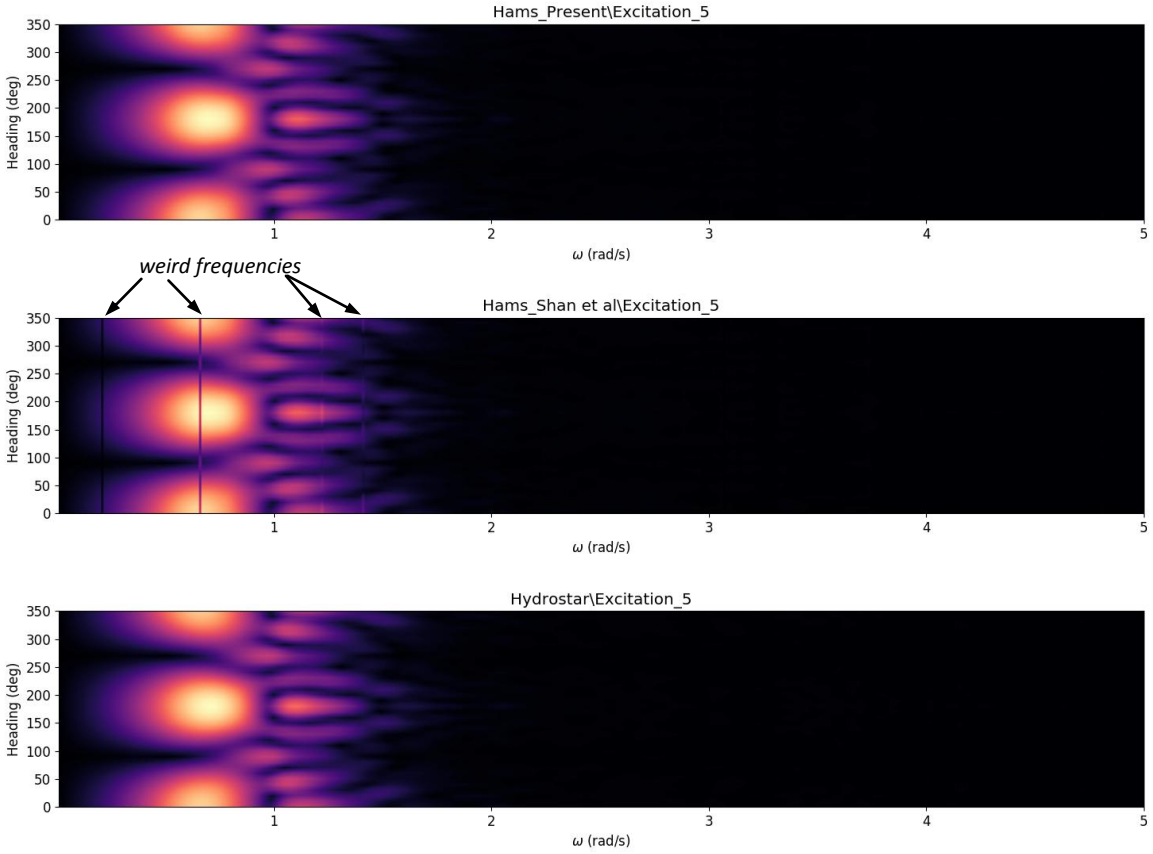

Fig. 13. Contour plots of the wave excitation force/moment (modulus) acting on the DeepCwind semisubmersible floater as a function of the wave angular frequency and the wave heading under a water depth of 50m: (a) surge wave excitation force, (b) heave wave excitation force and (c) pitch wave excitation moment. In the title of each subplot, 'Hams_Present', 'Hams_Shan et al' and 'Hydrostar' refer to the three computation methods aforementioned in Section 4.3.1 and 4.3.2, whilst the subscript after 'Excitation' stands for the DOF (degree of freedom) of the platform motion. The data are visualized using the commercial software StarViewer®.

(a)

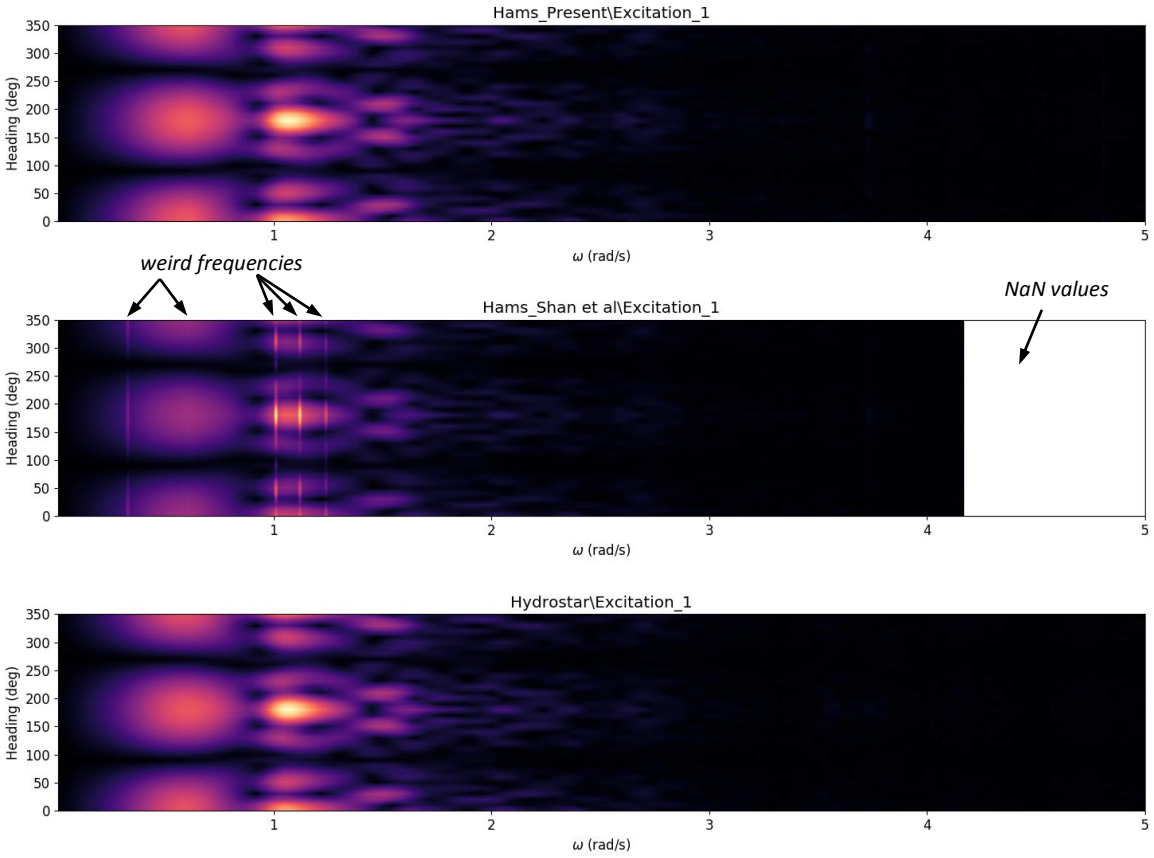
Hams_Present\Excitation_1
Heading (deg)
ω (rad/s)
weird frequencies
NaN values
Hams_Shan et al\Excitation_1
Heading (deg)
ω (rad/s)
Hydrostar\Excitation_1
Heading (deg)
ω (rad/s)

(b)

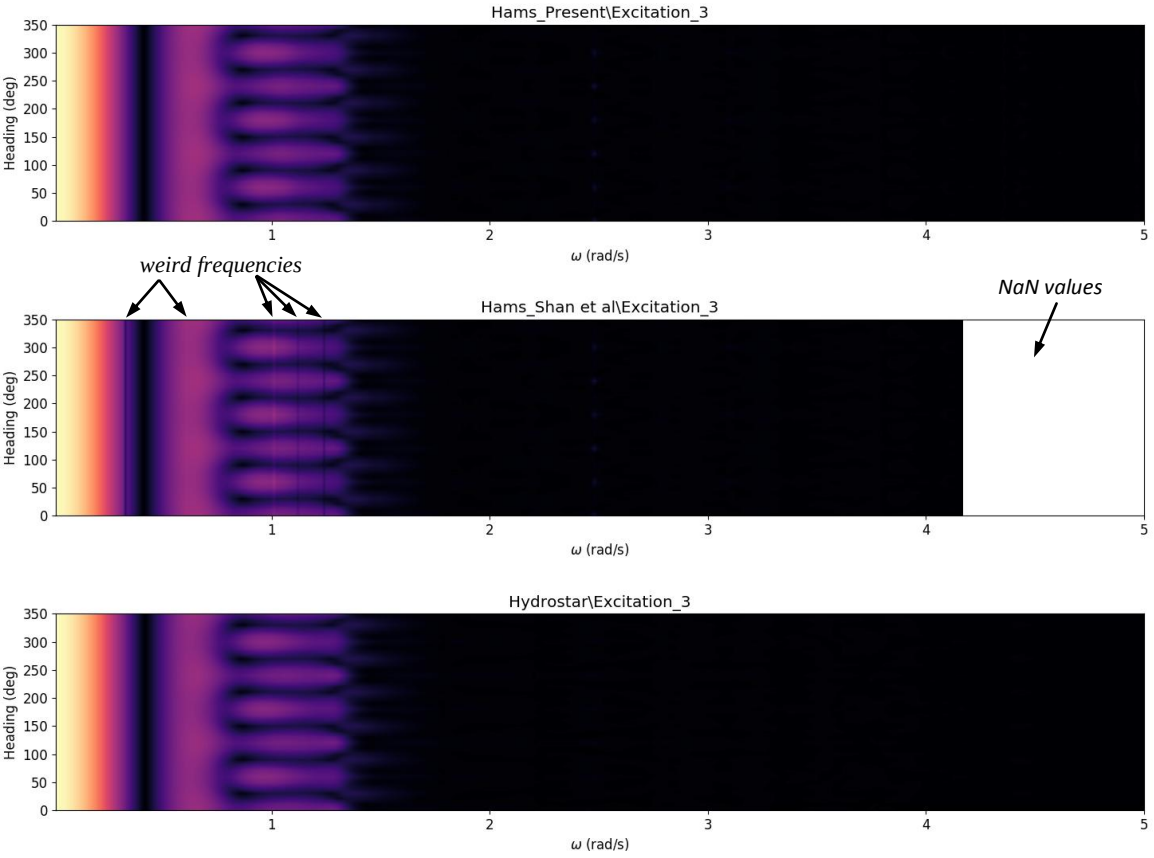
Hams_Present\Excitation_3
Heading (deg)
ω (rad/s)
weird frequencies
NaN values
Hams_Shan et al\Excitation_3
Heading (deg)
ω (rad/s)
Hydrostar\Excitation_3
Heading (deg)
ω (rad/s)

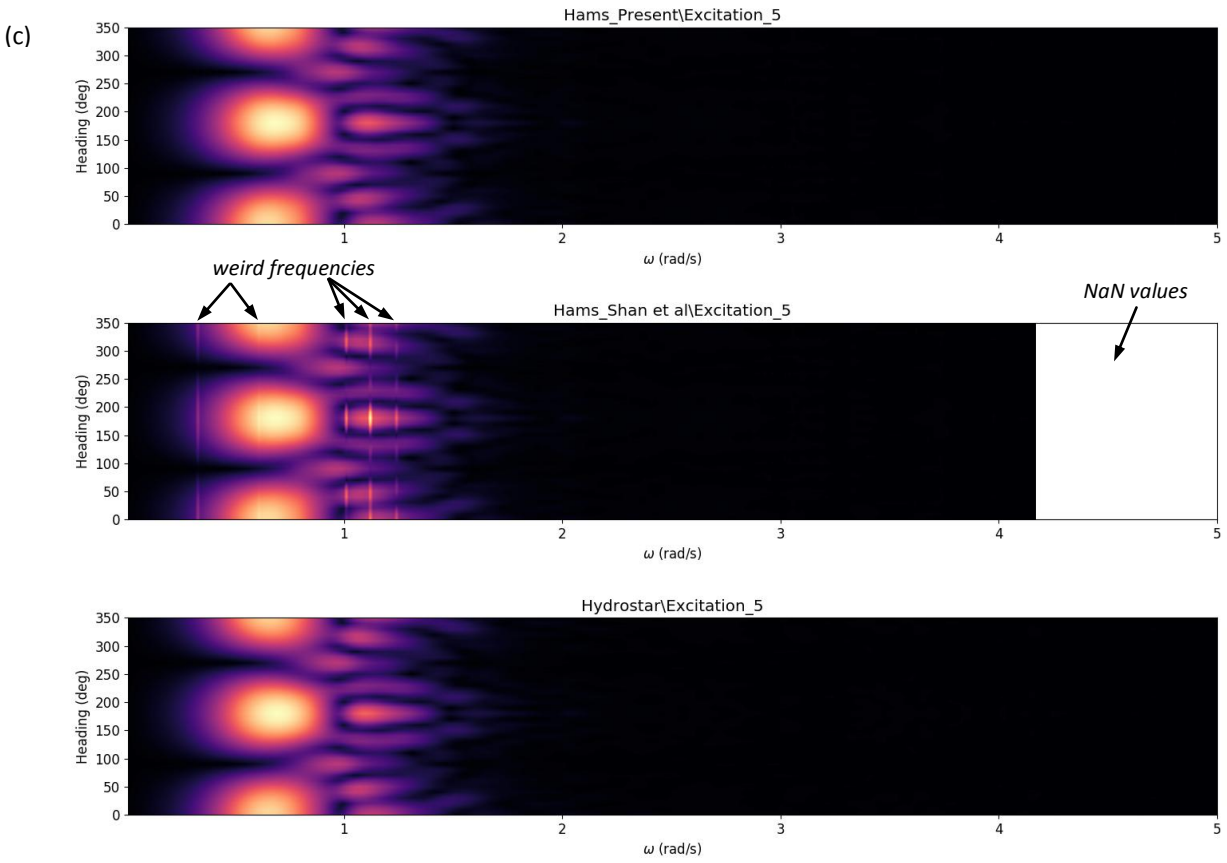

Fig. 14. Contour plots of the wave excitation force/moment (modulus) acting on the DeepCwind semisubmersible floater as a function of the wave angular frequency and the wave heading under a water depth of 200m: (a) surge wave excitation force, (b) heave wave excitation force and (c) pitch wave excitation moment. The data are visualized using the commercial software StarViewer®. Description of the subplot titles is given in Fig. 13.

Fig. 13 and Fig. 14 show contour plots of the wave excitation force/moment (modulus) acting on the DeepCwind semisubmersible floater, as a function of the wave angular frequency and the wave heading, under a water depth of 50m and 200m, respectively. First of all, the two figures clearly illustrate that by using Shan's algorithm (Shan et al., 2019), weird frequencies occur in the computed wave loads due to the problematic Green function's calculation. At these weird frequencies, the value of the wave excitation force/moment is surprisingly larger or smaller than its neighborhood within a quite limited frequency band. Secondly, under a large water depth (200 m in the present example), the computed wave loads show *NaN* values in a high-frequency region while it may not be the case for a small/mediate water depth. This can be attributed to the following two reasons: (1) a large water depth causes an overlarge parameter $k_0 h$ for the exponential integral $Ei(k_0 h)$, as indicated by Eq. (25) and described in Section 3.4; (2) an overlarge parameter $k_0 h$ exceeds the hardware's limitation in calculating hyperbolic functions such as $cosh(k_0 h)$, $cosh[k_0(z+h)]$ and $sinh\, 2k_0 h$, etc., existing in the expressions of the incident wave. Thanks to the present algorithm for evaluation of the Green function, the present numerical results are free from these problems, and good agreements are found in comparison to Hydrostar®'s results.

5. Conclusions

A newly-developed enhanced numerical algorithm for an accurate evaluation of the zero-forward speed free-surface Green function under a finite water depth has been presented, via a disposal of the singularities for incident waves of certain specific frequencies, a special treatment of the exponential integral with large para-meters and the elimination of nonsenses values in the high-frequency region. Comparison with Newman's polynomial algorithm in a variety of sea states confirms the accuracy of the present algorithm. By performing a benchmark test of the DeepCwind semisubmersible, through a comparison with Shan's algorithm (Shan et al., 2019) and the commercial software Hydrostar®, important findings can be summarized into the following aspects:

(1) Green's function and its partial derivatives calculated by Shan's algorithm (Shan et al., 2019) give incorrect values at some weird frequencies, in the circumstance when the abscissas of the Gauss-Laguerre quadrature occur closely near the singularities of the integrand.

(2) The loci of these weird frequencies depend on the *n*-node Gauss–Laguerre quadrature (*n* is selective) to be used. In other words, it solely relies on the loci of the roots of the *n*-node Laguerre polynomial $L_n(x)$. When a Gauss–Laguerre rule with a different order is applied, the loci of weird frequencies change.

(3) The contaminated frequency band of the computed wave loads near the weird frequencies is greatly affected by the size of the frequency step. Applying a relatively large frequency step can (though not completely) help to avoid the occurrence of the weird frequencies inherent in the original Endo's approach (Endo, 1987).

(4) Under a large water depth, the computed wave loads show *NaN* values in a high-frequency region, owing to the reason that the parameter k_0h is overlarge for the exponential integral $Ei(k_0h)$ and exceeds the hardware's limitation in calculating hyperbolic functions in the incident wave kinematics.

(5) The present algorithm is free from all the preceding problems, based on comparisons with Newman's polynomial algorithm and Hydrostar®'s computation results.

These findings are valuable to the subsequent researchers and the resultant new enhanced algorithm can contribute to consummate Endo's approach.

Acknowledgment

The financial support from the Grant-in-Aid for Early-Career Scientists (JSPS KAKENHI Grant Number JP18K13939), the Open Research Fund (Grant Number LP1815) of the State Key Laboratory of Coastal and Offshore Engineering (SKLCOE) of Dalian University of Technology, the Kyushu University Platform of Inter/Transdisciplinary Energy Research (Q-PIT) Support Program for Young Researchers (Grant Number 18112) and the Overseas Collaborative Research Program (Grant Number PJT-8) of the Japan Society of

Naval Architects and Ocean Engineers (JASNAOE) are gratefully acknowledged. The authors thank all the anonymous referees for their valuable comments on improving the manuscript.

Appendix. Partial derivatives of the Green's function

A.1 *The Rankine sources* ($\frac{1}{r}+\frac{1}{r_2}+G_0$)

In some higher-order BIEMs, the Rankine part is usually integrated with the wave term, using some special strategies for singular and near singular integrals (Sun et al. [37]). For this reason, it may also be necessary to calculate the Rankine sources, which can be treated in a single subroutine with a consistence form

$$Rankine(X,Y)=\{X^2+Y^2\}^{-1/2}, \tag{A1}$$

$$Rankine_X(X,Y)=-X*\{X^2+Y^2\}^{-3/2}=-X*\{Rankine(X,Y)\}^3, \tag{A2}$$

$$Rankine_Y(X,Y)=-Y*\{X^2+Y^2\}^{-3/2}=-Y*\{Rankine(X,Y)\}^3, \tag{A3}$$

where

$X=R,$ and $Y=z-\zeta,\ z+\zeta,\ z-\zeta-2h,\ z-\zeta+2h,\ z+\zeta+2h,\ z+\zeta+4h.$

A.2 *Partial derivatives of the integral* G_{11}

Note that the function $f_{11}(k)=[2v+(k+v)e^{-2kh}]$ is independent of the spatial coordinates R and z, therefore the two derivatives of G_{11} can be expressed by

$$G_{11R}=-\sum_{p=1}^{n}\frac{w_p}{h}\left[\frac{f_{11}(k_p)}{g(k_p)}-\frac{f_{11}(k_0)}{(k_p-k_0)g'(k_0)}\right]k_p e^{k_p(\zeta+z+h)}J_1(k_pR)+k_0F_X(X,Y)\frac{f_{11}(k_0)}{g'(k_0)}, \tag{A4}$$

$$G_{11z}=\sum_{p=1}^{n}\frac{w_p}{h}\left[\frac{f_{11}(k_p)}{g(k_p)}-\frac{f_{11}(k_0)}{(k_p-k_0)g'(k_0)}\right]k_p e^{k_p(\zeta+z+h)}J_0(k_pR)+k_0F_Y(X,Y)\frac{f_{11}(k_0)}{g'(k_0)}, \tag{A5}$$

where

$X=k_0R,$ and $Y=-k_0(z+\zeta).$

A.3 *Partial derivatives of the integrals* G_{12}, G_{13}, G_{14}

The two derivatives of G_{1i} $(i=2,3,4)$ can be expressed by

$$G_{1iR}=\sum_{p=1}^{n}\frac{w_p}{h}\left[\frac{f_{1iR}(k_p,R,z)}{g(k_p)}-\frac{f_{1iR}(k_0,R,z)}{(k_p-k_0)g'(k_0)}\right]-e^{-k_0h}Ei(k_0h)\frac{f_{1iR}(k_0,R,z)}{g'(k_0)}, \tag{A6}$$

$$G_{1iz}=\sum_{p=1}^{n}\frac{w_p}{h}\left[\frac{f_{1iz}(k_p,R,z)}{g(k_p)}-\frac{f_{1iz}(k_0,R,z)}{(k_p-k_0)g'(k_0)}\right]-e^{-k_0h}Ei(k_0h)\frac{f_{1iz}(k_0,R,z)}{g'(k_0)}, \tag{A7}$$

where

$$f_{12R}(k,R,z) = -kf_{11}(k)e^{-k(\zeta-z+h)}J_1(kR), \quad \text{(A8)}$$

$$f_{12z}(k,R,z) = kf_{11}(k)e^{-k(\zeta-z+h)}J_0(kR), \quad \text{(A9)}$$

$$f_{13R}(k,R,z) = -kf_{11}(k)e^{-k(z-\zeta+h)}J_1(kR), \quad \text{(A10)}$$

$$f_{13z}(k,R,z) = -kf_{11}(k)e^{-k(z-\zeta+h)}J_0(kR), \quad \text{(A11)}$$

$$f_{14R}(k,R,z) = -kf_{11}(k)e^{-k(\zeta+z+3h)}J_1(kR), \quad \text{(A12)}$$

$$f_{14z}(k,R,z) = -kf_{11}(k)e^{-k(\zeta+z+3h)}J_0(kR). \quad \text{(A13)}$$

References

Bayati, I., Gueydon, S., Belloli, M., 2015. Study of the effect of water depth on potential flow solution of the OC4 semisubmersible floating offshore wind turbine. *Energy Procedia* 80, 168-176.

Benitz, M.A., Schmidt, D.P., Lackner, M.A., Stewart, G.M., Jonkman, J.M., Robertson, A., 2015. Validation of hydrodynamic load models using CFD for the OC4-DeepCwind semisubmersible. In: *Proceedings of the ASME 2015 34th International Conference on Ocean, Offshore and Arctic Engineering*. St. John's, NL, Canada.

Chakrabarti, S.K., 2001. Application and verification of deepwater Green function for water waves. *Journal of Ship Research* 45, 187-196.

Chen, X.B., 1993. Evaluation de la fonction de Green du probleme de diffraction/radiation en profondeur d'eau finie-une nouvelle méthode rapide et précise, *Actes des 4e Journées de l'Hydrodynamique*, Nantes (France), 371–384.

Chen, X.B., 2004. Hydrodynamics in offshore and naval applications - Part I. In: *Proc. Of the 6th Intl. Conf. Hydrodynamics*, Perth, Australia.

Clément, A., 2013. A second order ordinary differential equation for the frequency domain Green function, in: *Proceedings of 28th International Workshop on Water Waves and Floating Bodies*, Marseille, France.

Endo, H., 1983. Numerical evaluation of principal value integral by Gauss-Laguerre quadrature. *AIAA Journal* 21,149-151.

Endo, H., 1987. Shallow-water effect on the motions of three-dimensional bodies in waves. *Journal of ship research* 31, 34-40.

John, F., 1950. On the motion of floating bodies II. *Communications on Pure and Applied Mathematics* 3, 45-101.

Li, L., 2001. *Numerical seakeeping predictions of shallow water effect on two ship interactions in waves*. Ph. D. thesis. Dalhousie University, Halifax, Canada.

Liang, H., Wu, H., Noblesse, F., 2018. Validation of a global approximation for wave diffraction-radiation in deep water. *Applied Ocean Research* 74, 80–86.

Linton, C.M., 1999. Rapidly convergent representations for Green functions for Laplace's equation. *Proceedings of The Royal Society A: Mathematical, Physical and Engineering Sciences* 455, 1767-1797.

Liu, R., Ren, H., Li, H., 2008. An improved Gauss–Laguerre method for finite water depth Green function and its derivatives. *Journal of Ship Mechanics* 12, 188–196.

Liu, Y., Iwashita, H., Hu, C., 2015. A calculation method for finite depth free-surface green function. International *Journal of Naval Architecture and Ocean Engineering* 7, 375-389.

Liu, Y., Hu, C., Sueyoshi, M., Iwashita, H., Kashiwagi, M., 2016. Motion response prediction by hybrid panel-stick models for a semi-submersible with bracings. *Journal of Marine Science and Technology* 21, 742-757.

Liu, Y., Yoshida, S., Hu, C., Sueyoshi, M., Sun, L., Gao, J., Cong, P., He, G., 2018a. A reliable open-source package for performance evaluation of floating renewable energy systems in coastal and offshore regions. *Energy Conversion and Management* 174, 516-536.

Liu, Y., Yoshida, S., Yamamoto, H., Toyofuku, A., He, G., Yang, S., 2018b. Response Characteristics of the DeepCwind Floating Wind Turbine Moored by a Single-Point Mooring System. *Applied Sciences* 8, 2306.

Liu, Y., 2019. HAMS: A Frequency-Domain Preprocessor for Wave-Structure Interactions—Theory, Development, and Application. *Journal of Marine Science and Engineering* 7, 81.

Mei, C.C., Stiassnie, M., Yue, D.K.P., 2005. *Theory and applications of ocean surface waves: nonlinear aspects*. World scientific.

Newman, J.N., 1985. Algorithms for free-surface Green function. *Journal of Engineering Mathematics* 19, 57-67.

Newman, J.N., 1986. Distributions of sources and normal dipoles over a quadrilateral panel. *Journal of Engineering Mathematics* 20, 113-126.

Newman, J.N., 1990. Numerical solutions of the water-wave dispersion relation. *Applied Ocean Research* 12, 14-18.

Newman, J.N., 1992. The approximation of free-surface Green functions. Retirement Meeting for Professor Fritz Ursell, University of Manchester, published in "*Wave Asymptotics*" edited by Martin PA and Wickham GR, pp. 107-135. Cambridge University Press.

Noblesse, F., 1982. The Green function in the theory of radiation and diffraction of regular water waves by a body. *Journal of Engineering Mathematics* 16, 137–169.

Peter, M.A., Meylan, M.H., 2004. The eigenfunction expansion of the infinite depth free surface Green function in three dimensions. *Wave Motion* 40, 1–11.

Pidcock, M.K., 1985. The calculation of Green functions in three dimensional hydrodynamic gravity wave problems. *International Journal for Numerical Methods in Fluids* 5, 891-909.

Ponizy, B., Noblesse, F., Ba, M., Guilbaud, M., 1994. Numerical evaluation of free-surface Green function. *Journal of Ship Research* 38, 193–202.

Press, W.H., Flannery, B.P., Teukolsky, S.A., Vetterling, W.T., 2007. *Numerical Recipes: The Art of Scientific Computing* (3rd ed.). Cambridge University Press.

Robertson, A., Jonkman, J.M., Masciola, M., Song, H., Goupee, A., Coulling, A., Luan, C., 2014. *Definition of the Semisubmersible Floating System for Phase II of OC4*. National Renewable Energy Laboratory (NREL), Golden, CO. Technical Report No NREL/TP-5000-60601.

Shan, P.H., Wu, J.M., 2018. Highly precise approximation of free surface Green function and its high order derivatives based on refined subdomains. *Brodogradnja/Shipbuilding* 69, 53–70.

Shan, P., Zhu, R., Wang, F., Wu, J., 2019. Efficient approximation of free-surface Green function and OpenMP parallelization in frequency-domain wave–body interactions. *Journal of Marine Science and Technology* 24, 479-489.

Sun, L., Teng, B., Liu, C.F., 2008. Removing irregular frequencies by a partial discontinuous higher order boundary element method. *Ocean Engineering* 35, 920-930.

Telste, J.G., Noblesse, F., 1986. Numerical evaluation of the Green function of water-wave radiation and diffraction. *Journal of Ship Research* 30, 69-84.

Wikipedia (accessed on Feb. 16, 2020): https://en.wikipedia.org/wiki/Gauss%E2%80%93Laguerre_quadrature

Wu, H., Zhang, C., Zhu, Y., Li, W., Wan, D., Noblesse, F., 2017. A global approximation to the Green function for diffraction radiation of water waves. *European Journal of Mechanics-B/Fluids* 65, 54-64.

Wu, H., Liang, H., Noblesse, F., 2018. Wave component in the Green function for diffraction radiation of regular water waves. *Applied Ocean Research* 81, 72-75.

Xie, C., Choi, Y., Rongère, F., Clément, A.H., Delhommeau, G., Babarit, A., 2018. Comparison of existing methods for the calculation of the infinite water depth free-surface Green function for the wave–structure interaction problem. *Applied Ocean Research* 81, 150-163.

Zhang, S., Jin, J.M., 1996. *Computation of special functions*. Wiley-Interscience.